UiO : Department of Mathematics
University of Oslo

Transit time and clogging of drops in constrictions

Richard Andre Fauli

Master's Thesis, Autumn 2019

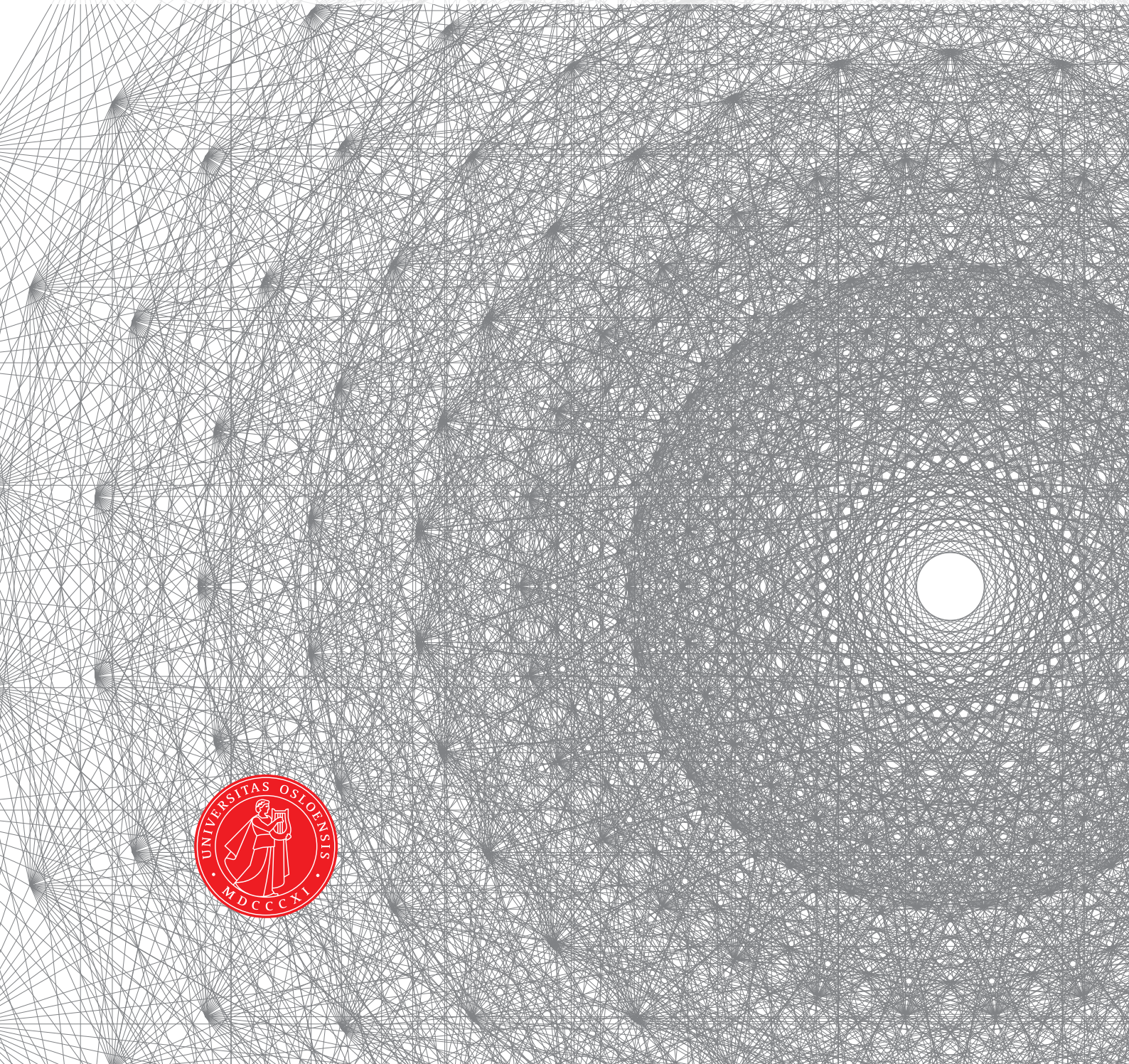

This master's thesis is submitted under the master's programme *Computational Science and Engineering*, with programme option *Mechanics*, at the Department of Mathematics, University of Oslo. The scope of the thesis is 60 credits.

The front page depicts a section of the root system of the exceptional Lie group E_8, projected into the plane. Lie groups were invented by the Norwegian mathematician Sophus Lie (1842–1899) to express symmetries in differential equations and today they play a central role in various parts of mathematics.

Abstract

In this thesis, results from numerical simulations and experiments on drops squeezing through constricted capillaries are presented. The purpose is to understand how the capillary number changes how drops are deformed as they pass through constrictions and how long it takes them to do so. The simulations use the Cahn–Hilliard phase-field model and the Stokes equations to simulate both simple and compound drops, which are solved using the finite element method with FEniCS. The numerical implementation is validated using test cases such as the spreading of a viscous drop and the Laplace pressure jump in a drop. For the experiments, simple drops were generated using microfluidics techniques and PDMS-chip manufacturing. Experiments with about 300 drops at low Reynolds numbers are presented. The numerical and experimental results do not initially show good agreement, but when changing the viscosity of the two liquids in the simulations the results become more similar. We discuss some possible reasons why the results are different, including the possibility that the boundary conditions on the drop could have been changed because of the use of surfactants. The transit time for simple and compound drops are found for a range of capillary numbers and numerical results show that as the capillary number is reduced, the way the drops are squeezed through the constriction changes and for sufficiently low capillary numbers both simple and compound drops clog the capillary.

Acknowledgements

First I would like to thank my supervisor associate professor Andreas Carlson for taking the time discuss the thesis with me almost every week despite us being in different countries for several months and him being on paternity leave the last few months. Also thank you to Christian Pedersen for much needed help with the FEniCS implementation in the beginning of this project and also for always having a positive outlook on things when I ask for your advice.

A big thanks to Dr. Joshua D. McGraw at ESPCI for invaluable help introducing me to microfluidics and being available whenever I needed help in the lab. Thank you to Dr. Alexandre Vilquin for invaluable help analyzing the experimental data. A big thank you also goes to UiO:LifeScience for funding my three month long visit to ESPCI and IPGG in Paris.

Last but not least I want to thank my family and friends for always being there and providing distractions such as volleyball, squash, video games and bouldering.

Richard Andre Fauli,
July 2019

Contents

List of Figures

List of Tables

CHAPTER 1

Introduction

Red blood cells transport oxygen to and carbon dioxide away from tissues. They can travel through capillaries with radii much smaller than that of the cell which they can do because they are flexible. In some circumstances, because the cell is too rigid or the forcing too small, the cell gets stuck blocking the flow which is known as capillary clogging. Some diseases such as malaria modify the red blood cells and reduce the deformability in both infected and uninfected cells [18, 54, 65] resulting in anemia. The World Health Organization estimated that 219 million cases of malaria occured in 2017 [74], so learning about the role of drop deformability in capillary clogging is important. There are also other cells that undergo similar deformations as they move through the body, for example when immune and cancer cells squeeze through tight constrictions the nuclear envelope can rupture and allow for nucleo-cytoplasmic mixing which can cause DNA damage [16, 59]. Understanding the squeezing dynamics of cells are also useful in the detection of circulating tumor cells which travel in blood to spread cancer [77, 82]. An increased understanding of both the dynamics that cause capillary clogging as well as cases were the cells are able to deform enough to pass through, are not only relevant for medical diagnostics [28], but have many other applications [79] such as drug delivery [61], enhanced oil recovery [53] and microfluidic droplet generation [26, 83]. This is the motivation for developing numerical simulations using the computational platform FEniCS [50] for drops passing through and/or clogging constrictions as well as designing and using an experimental setup to investigate these phenomena.

Investigation of drops and their dynamics can be traced back to the 1930s when G.I. Taylor expanded on the work of Einstein on the rheology of liquids with suspended solid particles, by replacing the solid particles with fluid drops [68]. He also looked at how drops deform in shear flow at low capillary numbers [67]. This was later expanded by Cox [13] to general time-dependent flows. Typically drops can be characterized as either simple or compound. Simple drops are liquid drops surrounded by a second liquid and compound drops are drops that consist of two liquid phases that are surrounded by a third liquid.

The motion of drops with radii greater or equal to tube radius in pressure driven pipe flow, is a problem which has been studied analytically [5, 29, 63], numerically [20, 42] and experimentally [57]. To characterize two-phase flow microfluidics, the relative importance of inertial, viscous, surface tension, buoyancy and gravitational forces as well as the ratio of densities ρ and viscosities η needs to be considered [26, 85]. The balance of the forces is expressed with the dimensionless numbers in Table 1.1. For the flow of blood in capillaries, were

Table 1.1: Overview of dimensionless parameters in two-phase microfluidic flow expressed with the viscosity of the continuous and dispersed phases η_c, η_d, characteristic velocity U, characteristic length scale L, surface tension σ and density of the continuous and dispersed phases ρ_c, ρ_d.

Dimensionless number	Formula	Definition
Capillary	$Ca = \frac{\eta_c U}{\sigma}$	$\frac{\text{Viscous forces}}{\text{surface tension forces}}$
Reynolds	$Re = \frac{\rho_c U L}{\eta_c}$	$\frac{\text{Inertial forces}}{\text{viscous forces}}$
Weber	$We = \frac{\rho_c U^2 L}{\sigma}$	$\frac{\text{Inertial forces}}{\text{surface tension forces}}$
Bond	$Bo = \frac{L^2 \Delta\rho g}{\sigma}$	$\frac{\text{Gravitational forces}}{\text{surface tension forces}}$
Viscosity ratio	$\eta = \frac{\eta_d}{\eta_c}$	$\frac{\text{Dispersed viscosity}}{\text{continuous viscosity}}$
Density ratio	$\rho = \frac{\rho_d}{\rho_c}$	$\frac{\text{Dispersed density}}{\text{continuous density}}$

typically the characteristic length and velocity scales are $L \sim 10$ μm and $U \sim 1$ mm/s [64] then gravitational, buoyancy and inertial forces becomes vanishingly small compared to viscous and surface tension forces. Which means the drop flow and deformation in a straight tube can be characterized with the capillary number Ca, viscosity ratio η and the relative drop size.

Since a natural extension of droplet flow in a straight tube is to look at tubes with a constriction, much of the work done on drop squeezing in constrictions builds on previous work on straight tubes. The constrictions are typically separated into two categories, short constrictions where the length of constriction is comparable to or shorter than drop size, and long constrictions are where the constriction length is much larger than the drop size. With a constricted geometry some new parameters needs to be introduced, such as the length and width of the constriction, as well as how the cross section, entrance and exit are shaped. Additionally, the wetting properties become more relevant since the drop is naturally pushed towards the tube walls as the cross-sectional area is reduced in the constriction.

Simple non-wetting drops being pushed through constrictions have been studied extensively analytically [41, 48, 62, 80, 81]. The problem has also been approached using numerical methods such as the volume of fluid method [78, 80–82], lattice–Boltzmann method [41], smoothed particle hydrodynamics method [75], boundary integral method [46] and hybrid boundary integral-mesh methods [62]. Simple drops being squeezed through constrictions have also been studied experimentally [12, 51] using microfluidic methods. Wetting drops have also been considered, but since there is no film between the drop and the walls [35] surface effects such as contact line pinning and static and dynamic friction complicates the system even further.

Zhang and colleagues have in last few years published several papers on viscous drops squeezing through short circular constrictions under constant flow rates. Assuming that there is only one phase in the radial direction because the film between the drop and the constriction wall is so thin and that the drop is spherical when it meets the constriction, they have developed an analytical framework which can predict the pressure profile [81] and minimum impulse [80] for a drop squeezing through constrictions. They have also studied circulating

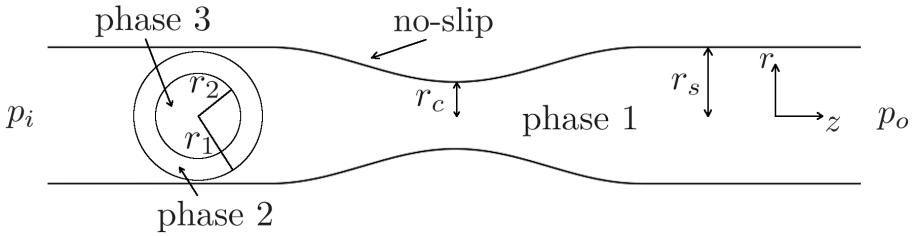

Figure 1.1: Illustration of a constriction geometry with a compound drop. p_i and p_o are inlet and outlet pressures, r_1 and r_2 are the radii of the outer and inner drop and r_c and r_s is the radius of the tube in the constriction and in the straight part.

tumour cells in microconfinements using the volume of fluid method [77, 78, 82] with constant flow rates.

Drops being driven by a constant pressure difference have been studied mostly numerically. Wu et al. [75] looked at how the deformability of a red blood cell relates to the pressure required to push the cell through a short triangularly narrowing constriction. Zinchenko and Davis [86] found using the boundary-integral method for a drop being driven by a constant pressure difference through a cubic lattice of spheres, an expression for the time it take to squeeze through as a function of capillary number Ca for viscosity ratios 1 to 4. They also concluded that while the viscosity ratio of the two fluids has almost no effect on the capillary number at which clogging occurs, it does have a strong effect on the squeezing dynamics.

Expanding from a simple drop to a compound drop, the system becomes considerably more complicated. And due to the increased complexity this has been mostly studied numerically. Phase-field methods [84], VOF [78] and the immersed boundary method [45] have been used. The focus has mainly been on constrictions that are much longer than the droplet size. We have not found experimental studies of compound drops squeezing through constrictions, but deformable capsules filled with liquid has been studied experimentally with constant flow rates for short constrictions [15, 55], were capsule elasticity controls the deformation instead of the surface tension.

The purpose of this thesis is to contribute to the understanding of the squeezing of simple and compound drops through constrictions. To achieve this, we study the problem using numerical simulations and experiments. Our focus will be on cases where the ratio of intertial and viscous forces, Re, is much smaller than one, which is what is typically found in blood flow. Further we will only consider axisymmetric geometries, illustrated in Figure 1.1. The tube radius r_s will be equal to or smaller than drop radius r_1 and constrictions will be short, which means the length of the constriction is about the size of the drops or shorter. For compound drops, the radius of the inner drop r_2 will be kept larger than the radius in the narrowest part of the constriction r_c. For simple drops $r_2 = 0$. We will mainly consider non-wetting droplets, and disregard any attractive or repulsive forces between the interface and wall.

We will approach to problem using numerical simulations and experiments. In the numerical part, we find the pressure and flow fields by solving the Stokes equations. To deal with interface dynamics we use the Cahn–Hilliard

(CH) phase field method, which is a diffuse-interface model which introduces the chemical potential μ and concentration ϕ that can be solved to find the surface tension forces. To solve the Stokes and CH equations, we use the finite element method (FEM) using FeniCS. In the experimental part, we will build an experimental setup using glass capillaries to make the constricted geometries and use microfluidic techniques to generate the drops.

In chapter 2 the theory needed for the numerical simulations is presented. We will discuss the Cahn–Hilliard (CH) equation, show how it was derived, show the 1D equilibrium profile, how the boundary conditions are expressed and coupling with hydrodynamic equations. In chapter 3 we go over the implementation of the CH and Stokes equations with the finite element method and discuss the mesh refinement we use on the interfaces. We then continue in chapter 4 by validating the FEM solver by comparing numerical results with several analytical solutions. In the next chapter the experimental methods we use are explained and we discuss the how drops are typically generated in microfluidics. In chapter 6 the results from both experiments and simulations will be presented, compared and discussed. Finally in chapter 7 we will make concluding remarks by discussing the limitations and the novelty of this work as well as discussing future work.

CHAPTER 2

Theory

2.1 Stokes equation

In order to study drops flowing through constrictions with blood flow in capillaries as a motivation, we first consider the parameters of capillary blood flow. Typical capillary diameters range from 5 to 10 μm, and blood has a dynamic viscosity of about 1 mPa·s and is slightly more dense than water at 1060 kg/m^3 [64]. Typical flow velocities are on the scale of millimeters per second. The resulting Reynolds number is on the order of $Re \sim 10^{-3}$.

At low shear rates, blood shows some non-Newtonian effects [64], but in our droplet model we will neglect these effects and assume the system to be Newtonian. Since the Reynolds number is so low the inertia terms of the Navier-Stokes equations are negligible and we therefore use the Stokes equations (2.1) to solve for the pressure p and velocity $\mathbf{u}$ fields.

$$\begin{aligned} -\nabla p + \nabla \cdot (\eta(\nabla \mathbf{u} + (\nabla \mathbf{u})^T)) + \mathbf{f} &= 0 \\ \nabla \cdot \mathbf{u} &= 0, \end{aligned} \tag{2.1}$$

where η is the dynamic viscosity and $\mathbf{f}$ is volume forces. The volume forces $\mathbf{f}$ is in this project the surface tension forces arising from the shape of the interface between the phases.

Since we are considering an axisymmetric system, we write the Eq. (2.1) in cylindrical coordinates on component form assuming that all parameters are constant with respect to rotation, and all angular components are zero:

$$0 = \frac{1}{r}\frac{\partial}{\partial r}(ru_r) + \frac{\partial u_z}{\partial z} \tag{2.2}$$

$$0 = -\frac{\partial p}{\partial r} + \frac{\partial}{\partial r}\left(\frac{\eta}{r}\frac{\partial}{\partial r}(ru_r)\right) + \frac{\partial}{\partial z}\left(\eta\frac{\partial u_r}{\partial z}\right) + f_r \tag{2.3}$$

$$0 = -\frac{\partial p}{\partial z} + \frac{1}{r}\frac{\partial}{\partial r}\left(\eta r\frac{\partial u_z}{\partial r}\right) + \frac{\partial}{\partial z}\left(\eta\frac{\partial u_z}{\partial z}\right) + f_z. \tag{2.4}$$

2.2 Phase-field formulation

In order to model multi-phase flows, a method for handling the interfaces as well as solving a hydrodynamic equation is needed. There are two main categories for

how interfaces are treated. The two categories are sharp- and diffuse-interface models [25, 52].

The sharp-interface methods [49, 70] can be divided into Eulerian surface capturing methods such as Volume of Fluid (VOF) and Level Set, and Lagrangian surface tracking methods such as the boundary-integral method. In the surface tracking methods mesh points follow the interface, which means the mesh is redrawn as the interface moves. The flow on each side of the interfaces are calculated with matching boundary condition on the interface. These methods typically have trouble with large movements of interfaces and drop breakup or coalescence [25]. For the capturing methods, the mesh does not need updating because of mesh movement since the location of the interface is found by solving for an interface function which captures the location the interfaces. One of the disadvantages of not changing the mesh according to the interface, is that the accuracy of the location of the interface is limited by the resolution in the area of the interface.

In this project we will not use a sharp-interface method, but instead the interface will be diffuse. The diffuse-interface methods are in a way an extension of the level set methods in that it instead of using an artificial smoothing function on the interface, the interface is a region of gradual transition between the phases on each side of the interface where mixing occurs. They also do not in principle require that the mesh be updated as the interfaces move. The are three main diffuse-interface methods [32]. The tracking/distributed force model and continuum surface force method, which are based on models of surface tension forces, and phase-field methods which are based on models of fluid free energy.

The diffuse-interface method we choose is the phase field method [2–4, 8, 10, 11, 32–34, 36–38, 40, 44, 76]. An order parameter or concentration ϕ is introduced to distinguish the phases. For two-phase flow, the concentration is $\phi = -1$ in one phase and $\phi = +1$ in the other. The interface is conventionally chosen to lie at the points where ϕ takes non-extremal values, and we will follow the convention that the interface is where $|\phi| < 0.9$. In addition to the order parameter we have the chemical potential μ as well, which is found by taking the functional derivative of the free energy functional $\mathscr{F}$ of the system. In the following we consider systems with only two phases.

Since interfaces are diffuse there are no discontinuities at the interface which aids in simplifying the numerical solution methods. When coupled with hydrodynamic equations, such as the Stokes equations, the volume force $\mathbf{f} = \mu\nabla\phi$ is used in equation (2.1) to add surface tension forces and the hydrodynamic equation can be solved in the entire system without needing to track or capture the interfaces such as in the sharp interface methods.

The main advantage of the phase-field methods is their versatility. They can be used to simulate complicated interface dynamics such as drop coalescence and breakup, which with surface tracking methods is difficult to do [49]. However because the interface is given a width they are best suited for modeling systems of small physical size.

Free energy formulation

The free energy per molecule f in a two-phase system, was expressed by Cahn and Hilliard [7] as a sum of two functions of the concentration and

concentration derivatives. They assumed that the gradient of ϕ was much smaller than than the reciprocal intermolecular distance and $\phi, \nabla\phi, \nabla^2\phi, ...$ were treated as independent variables. Then $f(\phi, \nabla\phi, \nabla^2\phi, ...)$ was expanded with a multivariate Taylor expansion about $f_0(\phi, 0, 0, ...)$ into

$$f(\phi, \nabla\phi, \nabla^2\phi, ...) = f_0(\phi) + k_1\nabla^2\phi + k_2(\nabla\phi)^2 + ... \tag{2.5}$$

where $k_1 = [\partial f/\partial\nabla^2\phi]_0$ and $k_2 = [\partial^2 f/(\partial|\nabla\phi|)^2]_0$, assuming that rotation and reflection about a four fold axis does not affect f. The total free energy density is $N_V f$, where N_V is the number of molecules per unit volume. The total free energy of a volume V is then

$$\mathscr{F} = N_V \int_V f dV = N_V \int_V \left(f_0(\phi) + k_1\nabla^2\phi + k_2(\nabla\phi)^2\right) dV.$$

Using the divergence theorem on the $\nabla^2\phi$ term, $\mathscr{F}$ can be written as a sum of the bulk free energy with a volume integral and the energy contribution from the external surface S with a surface integral

$$\mathscr{F} = N_V \int_V \left(f_0(\phi) + k(\nabla\phi)^2 + ...\right) dV + N_V \int_S \left(k_1\nabla\phi \cdot \mathbf{n}\right) dS, \tag{2.6}$$

where $k = k_2 - dk_1/d\phi$. Neglecting the higher order derivatives, the bulk free energy density can be written as

$$f_d = \left(\beta\Psi(\phi) + \frac{\alpha}{2}|\nabla\phi|^2\right), \tag{2.7}$$

where $\beta \sim \sigma/\epsilon$ and $\alpha \sim \sigma\varepsilon$ [10] with surface tension σ and interface thickness ε. The free energy density is split into two terms, the first representing the bulk energy in the two phases and the second being the interfacial energy. $\Psi(\phi)$ is defined as a double well potential with minima at $\phi = \pm 1$

$$\Psi(\phi) = \frac{1}{4}\left((\phi + 1)(\phi - 1)\right)^2, \tag{2.8}$$

shown in Figure 2.1. The free energy functional in the bulk is then

$$\mathscr{F}_V = \int_V \left(\beta\Psi(\phi) + \frac{\alpha}{2}|\nabla\phi|^2\right) dV. \tag{2.9}$$

To find the chemical potential μ of the system, the functional derivative of $\mathscr{F}_V$ is taken with respect to ϕ.

$$\delta\mathscr{F}_V = \int_V \left(\frac{\partial f_d}{\partial\phi}\delta\phi + \frac{\partial f_d}{\partial\nabla\phi} \cdot \delta\nabla\phi\right) dV,$$

using integration by parts on the second term we get

$$\delta\mathscr{F}_V = \int_V \left(\frac{\partial f_d}{\partial\phi} - \nabla \cdot \frac{\partial f_d}{\partial\nabla\phi}\right) \delta\phi dV + \int_S \mathbf{n} \cdot \frac{\partial f_d}{\partial\nabla\phi}\delta\phi dS.$$

Then inserting for f_d gives

$$\delta\mathscr{F}_V = \int_V \left(\beta\Psi'(\phi) - \alpha\nabla^2\phi\right) \delta\phi dV + \int_S \alpha\nabla\phi \cdot \mathbf{n}\delta\phi dS, \tag{2.10}$$

where $\Psi'(\phi) = \frac{d\Psi(\phi)}{d\phi}$. The chemical potential is recovered from the volume integral

$$\mu = \beta\Psi'(\phi) - \alpha\nabla^2\phi. \tag{2.11}$$

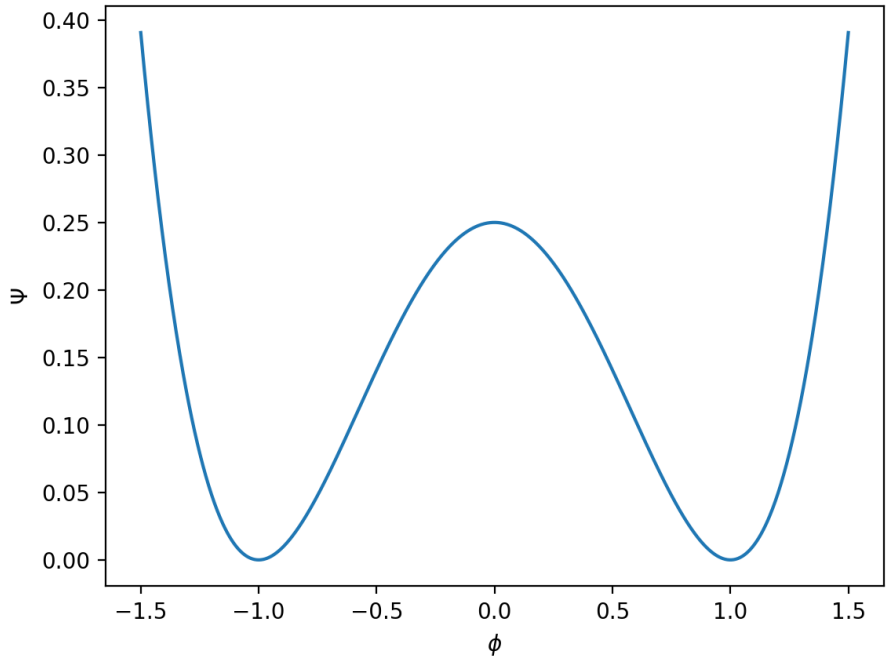

Figure 2.1: The double well potential $\Psi(\phi)$ with minima at $\phi = \pm 1$ which makes these points equilibrium states.

One dimensional case

The equilibrium profile of the interface can be found by minimizing the chemical potential. In one dimension this can done analytically. We begin by writing the expression for the chemical potential in one dimension where x is the normal direction to the interface

$$\mu = \beta\Psi'(\phi) - \alpha\frac{d^2\phi}{dx^2} = 0.$$

The expression is then multiplied by $d\phi/dx$ and integrated from $x = -\infty$ to x

$$\int_{-\infty}^{x}\left(\beta\Psi'(\phi)\frac{d\phi}{dx} - \alpha\frac{d^2\phi}{dx^2}\frac{d\phi}{dx}\right)dx = [\beta\Psi(\phi)]_{\phi=-1}^{\phi=\phi(x)} - \left[\frac{\alpha}{2}\left(\frac{d\phi}{dx}\right)^2\right]_{\phi=-1}^{\phi=\phi(x)} = 0,$$

where we have used that $\phi = -1$ far left of the interface. This can be written as

$$\beta\Psi(\phi) - \frac{\alpha}{2}\left(\frac{d\phi}{dx}\right)^2 = 0 \Rightarrow \frac{d\phi}{dx} = \pm\sqrt{\frac{2\beta}{\alpha}\Psi(\phi)}. \tag{2.12}$$

By requiring that $\phi \in [0, 1]$ and that $\phi(x)$ is monotonically increasing, the negative solution for $d\phi/dx$ may be discarded and the equation can be solved as a separable differential equation

$$\int_0^{\phi}\frac{d\phi}{\sqrt{\Psi(\phi)}} = \int_{x_0}^{x}\sqrt{\frac{2\beta}{\alpha}}dx.$$

First solving the integral on the left hand side gives

$$\int_0^\phi \frac{d\phi}{\sqrt{\Psi(\phi)}} = \int_0^\phi \frac{2d\phi}{(1-\phi)(1+\phi)} = \int_0^\phi \left(\frac{1}{1+\phi} + \frac{1}{1-\phi}\right) d\phi$$
$$= \left[\ln(1+\phi) - \ln(1-\phi)\right]_{\phi=0}^{\phi=\phi(x)} = \ln\left(\frac{1+\phi}{1-\phi}\right).$$

Solving the right hand using $x_0 = 0$ we get

$$\int_{x_0}^{x} \sqrt{\frac{2\beta}{\alpha}} dx = \sqrt{\frac{2\beta}{\alpha}} x,$$

which means that

$$\ln\left(\frac{1+\phi}{1-\phi}\right) = \sqrt{\frac{2\beta}{\alpha}} x.$$

By exponentiating both sides the expression can be simplified to

$$\frac{1+\phi}{1-\phi} = \exp\left(\sqrt{\frac{2\beta}{\alpha}} x\right) \Rightarrow \phi = \frac{\exp\left(\sqrt{\frac{2\beta}{\alpha}} x\right) - 1}{\exp\left(\sqrt{\frac{2\beta}{\alpha}} x\right) + 1} = \tanh\left(\sqrt{\frac{\beta}{2\alpha}} x\right),$$

which gives the one dimensional equilibrium profile $\phi_{1D}(x)$

$$\phi_{1D}(x) = \tanh\left(\frac{x}{\sqrt{2\varepsilon}}\right), \tag{2.13}$$

where we have used that $\alpha/\beta = \varepsilon$.

The effective surface tension in one dimension is defined by the integral [10]

$$\sigma = \alpha \int_{-\infty}^{\infty} \left(\frac{d\phi}{dx}\right)^2 dx = \frac{\sqrt{\alpha\beta}}{\sqrt{2}} \int_{-\infty}^{\infty} (1-\phi^2) d\phi = \frac{2\sqrt{2}}{3} \sqrt{\alpha\beta},$$

where we have substituted one of the $d\phi/dx$ factors using equation (2.12) and that $\phi(x = \pm\infty) = \pm 1$.

The equilibrium profile for the one dimenstional case is a good approximation for the profile in higher dimensions as well. In Figure 2.2 we show that equation (2.13) works well also in axisymmetry, where we plot the interface profile at equilibrium of an axisymmetric drop which was found numerically by initializing the drop with equation (2.13). When solving the CH equation in two or more dimensions and initializing using the 1D equilibrium profile, there is shift in the bulk value of ϕ, which depends on the relative size of the interface to the drop. This is a consequence of the fact that the 1D solution for the interface profile does not represent an energy minimum for higher dimensions [8, 76]. This results in a reduction of drop volume. Therefore some care has to be taken if we want to have a droplet of a certain volume in simulations. If the drop is too small compared to ε, the drop eventually disappears.

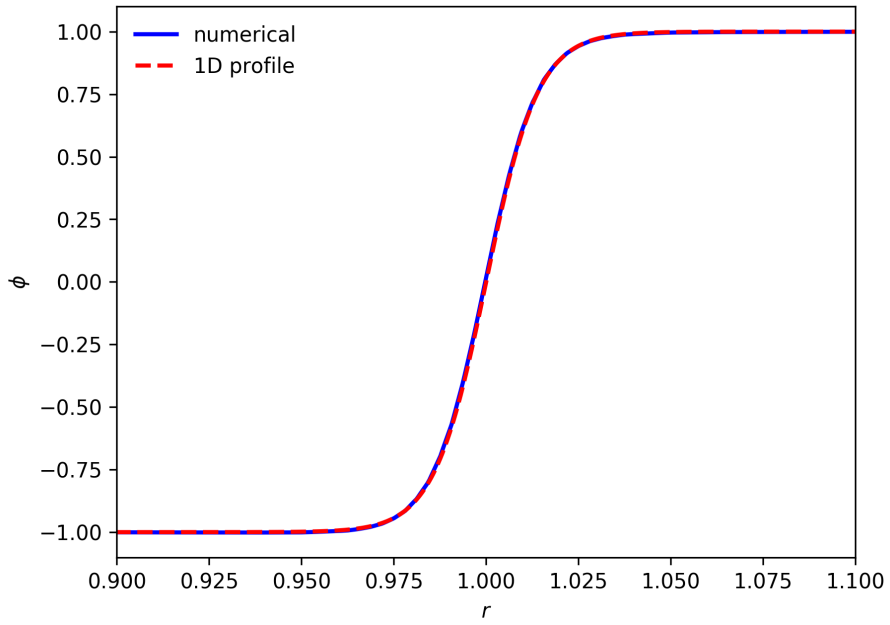

Figure 2.2: Plot of the one dimensional equilibrium profile given by equation (2.13) and the numerical equilibrium profile of an axisymmetric droplet initialized using equation (2.13) with a radius of 1.

Wetting Boundary conditions

The contribution to the total free energy from the surface can be postulated [11] as

$$\mathscr{F}_S = \int_S \left[\sigma_{sl} + (\sigma_{sg} - \sigma_{sl})w(\phi)\right] dS, \tag{2.14}$$

where σ_{sl} and σ_{sv} is the surface tension between the faces of solid (s), liquid (l) and gas (g). If the system we are looking at consists of two liquids and a solid, σ_{sg} is replaced with the surface tension between the second liquid and the solid. $w(\phi) = -\frac{1}{4}\phi^3 + \frac{3}{4}\phi + \frac{1}{2}$ is a normalized polynomial with $w(-1) = 0$, $w(1) = 1$ and $w'(-1) = w'(1) = 0$. Taking the variation of eq. (2.14) with respect to ϕ we get

$$\delta\mathscr{F}_S = \int_S (\sigma_{sg} - \sigma_{sl})w'(\phi)\delta\phi dS.$$

Collecting this boundary term and the boundary term in in eq. (2.10) we get the natural boundary condition for ϕ at the wall

$$\alpha\nabla\phi \cdot \mathbf{n} + (\sigma_{sg} - \sigma_{sl})w'(\phi) = 0.$$

Using the Young equation [43, p. 72] the contact angle θ_c can be introduced

$$\sigma\cos\theta_c = \sigma_{sg} - \sigma_{sl},$$

which means the boundary condition for ϕ can be written as

$$\nabla\phi \cdot \mathbf{n} + \frac{1}{\varepsilon}\cos\theta_c w'(\phi) = 0. \tag{2.15}$$

The boundary condition for ϕ is used to set the wetting properties of the system. This condition means that wherever there is a contact line, the contact angle is always constant. To account for non-equilibrium contact angles a term $D_w\partial\phi/\partial t$ can be added to the right hand side [11], where D_w is a phenomenological parameter. We will not take non-equilibrium contact angles into account, so the boundary condition will be as in equation (2.15).

For the chemical potential we impose there to be no fluxes of chemical potential through the boundaries which leads to

$$\nabla\mu \cdot \mathbf{n} = 0. \tag{2.16}$$

The Cahn–Hilliard equation

The Cahn–Hilliard (CH) equation is found by approximating interfacial diffusion fluxes as proportional to chemical potential gradients [32]. If there is a also a flow present, advection of the order parameter is also included which results in the CH equation with $\mathbf{u}$ as the the bulk velocity

$$\frac{\partial\phi}{\partial t} + \mathbf{u}\cdot\nabla\phi = \nabla\cdot[M(\phi))\nabla\mu] \tag{2.17}$$

where $M(\phi) = M$ is the mobility, which we will keep constant. For this model to be thermodynamically sound the free energy needs to decrease in time, so we need to make sure this is the case. If we consider the case where the bulk velocity $\mathbf{u} = 0$ equation (2.17) can be written as $\delta\phi = M\nabla^2\mu\,\delta t$ and since we have an equilibrium wetting boundary condition, the energy contribution from the boundary is zero. Inserting in the variation of $\mathscr{F}_V$ gives

$$\delta\mathscr{F}_V = \int_V \mu\,\delta\phi dV = \delta t\int_V \mu M\nabla^2\mu dV.$$

Using integration by parts and diving both sides with δt we get

$$\frac{\delta\mathscr{F}_V}{\delta t} = M\int_S \nabla^2\mu\,\nabla\mu\cdot\mathbf{n}dS - M\int_V(\nabla\mu)^2\,dV = -M\int_V(\nabla\mu)^2\,dV,$$

where the boundary term is zero because of the chemical potential boundary condition. To ensure decrease of free energy the mobility constant must therefore be positive.

In addition to being useful in multi-phase flow simulations, there are several other applications [40] such as spinodal decomposition, diblock copolymer and image inpainting.

2.3 Coupling Stokes and CH for two-phase flow

To couple the CH equation and the Stokes equation, the surface tension force $\mathbf{f} = -\mu\nabla\phi$ [32] is added to the right hand side of the Stokes equation, modifying it to

$$\nabla p = \nabla\cdot(\eta(\nabla\mathbf{u} + (\nabla\mathbf{u})^T)) - \mu\nabla\phi. \tag{2.18}$$

Another choice for the surface tension is using $\mathbf{f} = -\phi\nabla\mu$, but this requires a the use of a modified pressure [11, 32].

Non-dimensionalization

Before implementing these equations, we first make them non-dimensional. We introduce characteristic parameters and non-dimensional numbers following [10] and take into account that we have creeping flow. The dimensionless variables are with superscript *

$$x = Lx^*, \quad t = \frac{L}{U}t^*, \quad p = \frac{\eta U}{L}p^*, \quad u = Uu^*, \quad \mu = \frac{3\sigma}{2\sqrt{2}\epsilon}\mu^*, \tag{2.19}$$

where L is the characteristic length scale, U is the characteristic velocity, ϵ the interface width and σ is the surface tension. When we later look at drops in capillaries, we use the capillary radius as characteristic length scale, $L = r_s$ and the drop velocity as the characteristic velocity.

By using these and arranging the expressions appropriately we end up with the following non-dimensional system of differential equations, where now the superscript * is omitted,

$$\nabla \cdot \mathbf{u} = 0 \tag{2.20}$$

$$\nabla p = \nabla \cdot \left(\lambda(\eta,\phi)(\nabla\mathbf{u} + (\nabla\mathbf{u})^T)\right) - \frac{\mu\nabla\phi}{Cn \cdot Ca} \tag{2.21}$$

$$\frac{\partial\phi}{\partial t} + \mathbf{u}\cdot\nabla\phi = \frac{1}{Pe}\nabla^2\mu = \frac{1}{Pe}\nabla^2\left[F'(\phi) - Cn^2\nabla^2\phi\right], \tag{2.22}$$

where $\lambda(\eta,\phi)$ is a linear function of ϕ with $\lambda(\eta,-1) = \eta$ and $\lambda(\eta,1) = 1$

$$\lambda(\eta,\phi) = \frac{1+\phi+\eta(1-\phi)}{2}$$

and η is now the viscosity ratio. The non-dimensional numbers are the Peclet (Pe) number which is the ratio of advection and diffusion, the Cahn (Cn) number which is the ratio of the interface width and characteristic length scale and the capillary number (Ca) which is the ratio of viscous and surface tension forces

$$Pe = \frac{2\sqrt{2}U\epsilon L}{3M\sigma}, \qquad Cn = \frac{\varepsilon}{L}, \qquad Ca = \frac{2\sqrt{2}\eta_c U}{3\sigma},$$

where η_c is the dynamic viscosity of the continuous phase. With these parameters, the one dimensional equilibrium profile (2.13) is written on non-dimensional form as

$$\phi_{1D} = \tanh\left(\frac{x}{\sqrt{2}Cn}\right). \tag{2.23}$$

The two main modeling parameters that we set in the simulations are the interface width and mobility, using the non-dimensional numbers these are determined by Cn and Pe respectively. Since ε in the simulations can be orders of magnitude larger than the physical interface which $\sim 10^{-9}$ m [52], the mobility parameter can typically be $\sim 10^{-17}$ m^{3}s kg^{-1} [33, 52]. Using such

low numbers for example for a characteristic length scale of a $L = 1$ mm we would need to set $Cn = 10^{-6}$, which would need a too high mesh resolution to solve. Because the interface has to be width has to be higher in the simulations than in reality, Pe has to be adjusted accordingly. The sharp-interface limit is where the relation between Cn and Pe is properly set such that the convection and capillary stresses on the diffuse interface can be modeled reasonably [21, 52]. To find this relation, asymptotic expansions for the interface and the two fluids can be done, where inner solutions are expanded with the parameter $1/Pe$ and the outer solution with the parameter Cn^2Pe. By requiring that the inner and outer solutions should both rely on the same parameter, Magaletti and colleagues [52] found that

$$\frac{1}{Pe} = Cn^2 Pe \ll 1,$$

which reduces to

$$Pe \propto \frac{1}{Cn}.$$

Further, Magaletti et al. confirm the inverse proportionality by numerical experiments of capillary waves and drop coalescence. They suggest a prefactor to achieve convergence to the sharp interface limit

$$Pe \simeq \frac{1}{3Cn}, \tag{2.24}$$

which is how Pe is set for all of the simulations in this project.

Since we are studying an axisymmetrical system we write the non-dimensional CH and Stokes equations (2.20, 2.21, 2.22) on axisymmetrical form by using that $\partial/\partial\theta = u_\theta = 0$. This gives us the system of partial differential equations (PDEs) we want to solve

$$0 = \frac{1}{r}\frac{\partial}{\partial r}(ru_r) + \frac{\partial u_z}{\partial z} \tag{2.25}$$

$$0 = -\frac{\partial p}{\partial r} + \frac{\partial}{\partial r}\left(\frac{\lambda}{r}\frac{\partial}{\partial r}(ru_r)\right) + \frac{\partial}{\partial z}\left(\lambda\frac{\partial u_r}{\partial z}\right) + f_r \tag{2.26}$$

$$0 = -\frac{\partial p}{\partial z} + \frac{1}{r}\frac{\partial}{\partial r}\left(\lambda r\frac{\partial u_z}{\partial r}\right) + \frac{\partial}{\partial z}\left(\lambda\frac{\partial u_z}{\partial z}\right) + f_z \tag{2.27}$$

$$f_r = -\frac{\mu}{Cn\cdot Ca}\frac{\partial\phi}{\partial r}, \qquad f_z = -\frac{\mu}{Cn\cdot Ca}\frac{\partial\phi}{\partial z} \tag{2.28}$$

$$\frac{\partial\phi}{\partial t} + u_r\frac{\partial\phi}{\partial r} + u_z\frac{\partial\phi}{\partial z} = \frac{1}{Pe}\left(\frac{1}{r}\frac{\partial}{\partial r}\left(r\frac{\partial\mu}{\partial r}\right) + \frac{\partial^2\mu}{\partial z^2}\right) \tag{2.29}$$

$$\mu = \Psi'(\phi) - Cn^2\left(\frac{1}{r}\frac{\partial}{\partial r}\left(r\frac{\partial\phi}{\partial r}\right) + \frac{\partial^2\phi}{\partial z^2}\right). \tag{2.30}$$

Energy evaluations

Since we are studying flow dominated by viscous forces, viscous dissipation should play a major role in how energy is lost in the system. The viscous dissipation rate $\dot{R}_\eta$ and the rate of diffusive fluxes of the chemical potential $\dot{R}_\mu$

can be calculated and scaled with the surface energy [9]. The rate of viscous dissipation is given by

$$\dot{R}_\eta = \int_V Ca\lambda \nabla \mathbf{u} : \left(\mathbf{u} + \nabla^T \mathbf{u}\right) dV,$$

which on axisymmetrical form becomes

$$\begin{aligned}\dot{R}_\eta = \int_V Ca\lambda \Bigg(& 2\left(\frac{\partial u_r}{\partial r}\right)^2 + \left(\frac{\partial u_r}{\partial z}\right)^2 + 2\frac{\partial u_r}{\partial z}\frac{\partial u_z}{\partial r} \\ & + 2\left(\frac{u_r}{r}\right)^2 + \left(\frac{\partial u_z}{\partial r}\right)^2 + 2\left(\frac{\partial u_z}{\partial z}\right)^2 \Bigg) dV,\end{aligned} \tag{2.31}$$

and the rate of diffusive fluxes of chemical potential is

$$\dot{R}_\mu = \int_V \frac{Cn}{Pe}\left(\frac{\partial \mu}{\partial t}\right)^2 dV. \tag{2.32}$$

Since there is no inertia in our model, $Re \ll 1$, the rate of change in kinetic energy will be very small, and because our wetting boundary condition does not allow for non-equilibrium contact angles, dissipation due to contact line relaxation is not a factor. The surface free energy can also be found by calculating the interface surface area since the surface free energy is proportional to the surface area.

2.4 Three-phase flow

The model we have discussed so far is only for two-phase flow. Compound drops can be studied with this model, but it would be limited to drops that have the same surface tension on the inner and outer interface, since with a two-phase model the inner liquid would be the same as the outer. To have compound drops that allow for interfaces with different surface tensions and different viscosities for all three phases, the CH–Stokes model has to be modified to include a third phase.

There are two ways to expand the model to include a third phase. The more rigorous method, but also more complex is to use a ternary Cahn–Hilliard model [3, 4, 39]. In these ternary models, a new expression for the free energy has to be introduced which also means the expression for the chemical potential also changes. In some ternary models the free energy functional $\mathscr{F}_3$ and chemical potential μ_i can be written as [39]

$$\begin{aligned}\mathscr{F}_3 &= \int_V \left(\frac{1}{4}\sum_{i=1}^{3}\phi_i^2(1-\phi_i)^2 + \frac{\varepsilon^2}{2}\sum_{i=1}^{3}|\nabla\phi_i|^2\right) dV \\ \mu_i &= \frac{1}{4}\frac{\partial\left(\sum_{i=1}^{3}\phi_i^2(1-\phi_i)^2\right)}{\partial\phi_i} - \varepsilon^2\nabla^2\phi_i + \beta(\phi_1,\phi_2,\phi_3),\end{aligned}$$

where $\beta(\phi_1, \phi_2, \phi_3)$ is a non-constant Lagrange-multiplier which makes sure that the sum of the chemical potentials is zero. In these models, the concentration $\phi_i \in [0, 1]$ and $\phi_1 + \phi_2 + \phi_3 = 1$. In phase i, $\phi_i = 1$ and $\phi_j = 0$ for $j \neq i$. If

we were to choose a ternary Cahn–Hilliard model of this type, the CH solver would have to be substantial changed.

Another method, is to have two CH equations, one to govern phases 1 and 2 and the other for phases 2 and 3, each with their respective chemical potentials μ_1 and μ_2 and concentrations ϕ_1 and ϕ_2. The surface tension term in the momentum equation (2.28) is also expanded to include the second interface. The system of PDEs that we end up with is very similar to the two-dimensional case:

$$0 = \frac{1}{r}\frac{\partial}{\partial r}(ru_r) + \frac{\partial u_z}{\partial z} \tag{2.33}$$

$$0 = -\frac{\partial p}{\partial r} + \frac{\partial}{\partial r}\left(\frac{\lambda}{r}\frac{\partial}{\partial r}(ru_r)\right) + \frac{\partial}{\partial z}\left(\lambda\frac{\partial u_r}{\partial z}\right) + f_r \tag{2.34}$$

$$0 = -\frac{\partial p}{\partial z} + \frac{1}{r}\frac{\partial}{\partial r}\left(\lambda r\frac{\partial u_z}{\partial r}\right) + \frac{\partial}{\partial z}\left(\lambda\frac{\partial u_z}{\partial z}\right) + f_z \tag{2.35}$$

$$f_r = -\frac{\mu_1}{Cn\cdot Ca_1}\frac{\partial\phi_1}{\partial r} - \frac{\mu_2}{Cn\cdot Ca_2}\frac{\partial\phi_2}{\partial r} \tag{2.36}$$

$$f_z = -\frac{\mu_1}{Cn\cdot Ca_1}\frac{\partial\phi_1}{\partial z} - \frac{\mu_2}{Cn\cdot Ca_2}\frac{\partial\phi_2}{\partial z} \tag{2.37}$$

$$\frac{\partial\phi_1}{\partial t} + u_r\frac{\partial\phi_1}{\partial r} + u_z\frac{\partial\phi_1}{\partial z} = \frac{1}{Pe}\left(\frac{1}{r}\frac{\partial}{\partial r}\left(r\frac{\partial\mu_1}{\partial r}\right) + \frac{\partial^2\mu_1}{\partial z^2}\right) \tag{2.38}$$

$$\frac{\partial\phi_2}{\partial t} + u_r\frac{\partial\phi_2}{\partial r} + u_z\frac{\partial\phi_2}{\partial z} = \frac{1}{Pe}\left(\frac{1}{r}\frac{\partial}{\partial r}\left(r\frac{\partial\mu_2}{\partial r}\right) + \frac{\partial^2\mu_2}{\partial z^2}\right) \tag{2.39}$$

$$\mu_1 = \Psi'(\phi_1) - Cn^2\left(\frac{1}{r}\frac{\partial}{\partial r}\left(r\frac{\partial\phi_1}{\partial r}\right) + \frac{\partial^2\phi_1}{\partial z^2}\right) \tag{2.40}$$

$$\mu_2 = \Psi'(\phi_2) - Cn^2\left(\frac{1}{r}\frac{\partial}{\partial r}\left(r\frac{\partial\phi_2}{\partial r}\right) + \frac{\partial^2\phi_2}{\partial z^2}\right) \tag{2.41}$$

The only connection between the two sets of CH equations is the velocity, so any interaction between the interfaces in this model is strictly limited to how their respective surface tension terms in the momentum equations (2.34) and (2.35) affect the velocity field. Since the first set of CH equations (2.38) and (2.40) only considers phases 1 and 2 and the second set (2.39) and (2.41) considers phases 2 and 3, this model can only be used for cases where phases 1 and 3 have no shared interface. This considerably limits the types of cases this model can be used to investigate, for example the collision of two drops of different phases dispersed in a third continuous phase can not be studied. However for the case of a compound drop being squeezed through a constriction, we do not expect this limitation to cause problems.

To illustrate how the three-phase model is used we will consider a one-dimensional case. We initialize ϕ_1 and ϕ_2 with the equilibrium profile given by equation (2.23), shifted so that the interfaces are separated by one characteristic length scale. When the system has reached equilibrium, ϕ_1, ϕ_2 and $\phi_1 + \phi_2$ is as shown in Figure 2.3. To interpret the three-phase system, the solutions for ϕ_1 and ϕ_2 are added together and phase 1 is where $\phi_1 + \phi_2 = -2$, phase 2 is where $\phi_1 + \phi_2 = 0$ and phase 3 is where $\phi_1 + \phi_2 = 2$. The two interfaces are located where ϕ is around either -1 or 1.

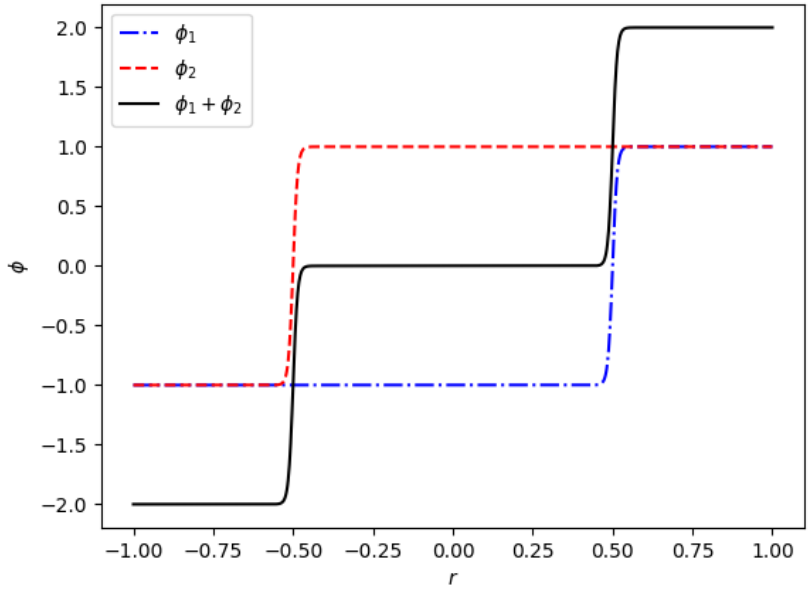

Figure 2.3: Profiles of ϕ_1, ϕ_2 and $\phi_1 + \phi_2$ for the three-phase model. ϕ_1 and ϕ_2 is the solution from each CH equation, and $\phi_1 + \phi_2$ gives the location of the three phases and interfaces.

CHAPTER 3

Numerical implementation

3.1 Finite Element Method

In order to solve them system of PDEs in the CH–Stokes models we use the finite element method (FEM). FEM is a method for finding approximate solutions to PDEs, where the domain is divided into elements and on each element there is a set of nodes [50]. The nodes that are on the boundaries between elements are the shared nodes and internal nodes are those located on the inside of an element. For each node i there is a finite element basis function ψ_i. These finite element basis functions are called trial functions, and with FEM we seek solutions written as linear combinations of these trial functions. The PDEs we want to solve need to be written on weak form, which is done by multiplying the PDE with a test function and integrating over the domain. Usually the test functions are the same as the trial functions, which is also the case for this project.

Weak formulation

In order to write the PDEs on weak form, the equations are multiplied with a test function and integrated over the domain Ω. The Neumann boundary conditions given by equations (2.15) and (2.16), appear when integration by parts is done on second order derivatives of ϕ, μ, u_r and u_z. In the following we will show the weak formulation for the two-phase CH–Stokes model.

The weak form for the continuity equation (2.25) is found by multiplying with the test function $l(r, z) = l$ and integrating over the domain

$$\int_\Omega \left(\frac{1}{r}\frac{\partial}{\partial r}(ru_r) + \frac{\partial u_z}{\partial z} \right) l d\Omega = 0,$$

where $d\Omega = rdrdz$, which means the continuity equation on weak form is

$$\int_\Omega \left(\frac{\partial}{\partial r}(ru_r) + r\frac{\partial u_z}{\partial z} \right) l dr dz = 0. \tag{3.1}$$

For the r-component of the Stokes equations (2.26) we multiply with $k_r r$, where $k_r(r, z) = k_r$ is the test function. The reason we also multiply the equation with r is to avoid terms with $1/r$ in the weak form. The two terms containing u_r are also partially integrated, which results in the following expression for

the weak form

$$\begin{aligned} -\int_\Omega \lambda \left[\frac{\partial}{\partial r}(ru_r) \left(2k_r + r\frac{\partial k_r}{\partial r} \right) + \frac{\partial u_r}{\partial z}\frac{\partial k_r}{\partial z} r^2 \right] drdz \\ + \int_\Omega \left(-\frac{\partial p}{\partial r}k_r + \frac{\mu}{Cn \cdot Ca}\frac{\partial \phi}{\partial r}k_r \right) r^2 drdz \\ + \int_{\partial\Omega} \left(u_r + \frac{\partial u_r}{\partial r} r \right) k_r r dz + \int_{\partial\Omega} \frac{\partial u_r}{\partial z} k_r r^2 dr = 0, \end{aligned} \tag{3.2}$$

where $\partial\Omega$ means it is a boundary integral. For the z-component (2.27) we multiply with the test function $k_z(r,z) = k_z$ and partially integrate the two terms with u_z to get the weak form

$$\begin{aligned} -\int_\Omega \left[\lambda \left(\frac{\partial u_z}{\partial r}\frac{\partial k_z}{\partial r} + \frac{\partial u_z}{\partial z}\frac{\partial k_z}{\partial z} \right) + \frac{\partial p}{\partial z}k_z - \frac{\mu}{Cn \cdot Ca}\frac{\partial \phi}{\partial z}k_z \right] rdrdz \\ + \int_{\partial\Omega} r\frac{\partial u_z}{\partial r}k_z dz + \int_{\partial\Omega} \frac{\partial u_z}{\partial z}k_z r dr = 0. \end{aligned} \tag{3.3}$$

The weak forms for the CH equations (2.29) and (2.30), is found by multiplying the equations with the test functions $q(r,z) = q$ and $v(r,z) = v$ respectively and then integrating over the domain. The terms containing derivatives of μ or ϕ are partially integrated which gives the following weak forms

$$\begin{aligned} \int_\Omega \left[\left(\frac{\partial \phi}{\partial t} + u_r\frac{\partial \phi}{\partial r} + u_z\frac{\partial \phi}{\partial z} \right) q - \frac{1}{Pe}\left(\frac{\partial \mu}{\partial r}\frac{\partial q}{\partial r} - \frac{\partial \mu}{\partial z}\frac{\partial q}{\partial z} \right) \right] rdrdz \\ + \int_{\partial\Omega} \frac{\partial \mu}{\partial r} qrdz + \int_{\partial\Omega} \frac{\partial q}{\partial z} qrdr = 0, \end{aligned} \tag{3.4}$$

$$\begin{aligned} \int_\Omega \left[(\mu v - F'(\phi))\, v - Cn^2 \left(\frac{\partial \phi}{\partial r}\frac{\partial v}{\partial r} + \frac{\partial \phi}{\partial z}\frac{\partial v}{\partial z} \right) \right] rdrdz \\ + Cn^2 \int_{\partial\Omega} \frac{\partial \phi}{\partial r} vrdz + Cn^2 \int_{\partial\Omega} \frac{\partial \phi}{\partial z} vrdr = 0. \end{aligned} \tag{3.5}$$

The weak formulation for the PDEs in the three-phase CH–Stokes model is similar to the two-phase one. The only difference is an extra set of CH equations and an extra term in the momentum equations (3.2) and (3.3).

Neumann boundary conditions are applied using the boundary integral terms. For example if we want to impose a contact angle θ_c on a surface with normal vector $\mathbf{n} = \mathbf{i_z}$ we use

$$\frac{\partial \phi}{\partial z} = -\frac{2}{Cn}\cos\theta_c w'(\phi).$$

For both the two- and three-phase models, the CH and Stokes equations are separated into two systems. We first solve the CH equations using the velocity field from the previous time step and then we solve Stokes equations using the solutions from the CH equations. For the time differentiation in the CH equations the backward euler scheme is used. The elements we use for the Stokes equations are Taylor-Hood elements, which have Lagrangian polynomials of order q for u and $q-1$ for p for $q \geq 2$ as basis element functions

[50]. In our case we use elements with $q = 2$. For the CH equation, we use linear Lagrangian polynomials for both μ and ϕ. To solve these equations, we use the built-in Newton solver in FEniCS with the linear solver MUMPS using standard parameters which means the relative tolerance is 10^{-9} and the absolute tolerance is 10^{-10}. The use of FEniCS will be further discussed in the next section.

3.2 FEniCS

To solve the PDEs we have, we use the FEniCS platform [50]. FEniCS is an open-source computational platform which endeavors to automate the process of solving PDEs using FEM. FEniCS can be used with both Python and C++, but in this project we have chosen to only use Python with FEniCS. Some of the scripts can be found in the github repository Squeezing-of-drops-through-constrictions [24]. There are several reasons why FEniCS has been chosen. It is quick to implement changes as the input used is close to the mathematical form, it is efficient and the same code which is run on a single core on a laptop can be run in parallel on many cores by simply calling the program in a slightly different way. In this project however, we found through experimentation that without making significant changes to the code the scaling in parallel was poor. We therefore decided not to use the parallel functionality in FEniCS, but instead run several simulations with different parameters at the same time. The majority of the simulations were done on the abacus-as machine at the Department of Mathematics at the University of Oslo.

To solve the Stokes and CH equations in FEniCS the weak forms are expressed as SL and CHL by adding the left hand sides of equations (3.1, 3.2, 3.3 and 3.4, 3.5) shown below in Python notation.

```
# Stokes
# r - component:
L0 = -Dx(p, 0) * k[0] * r**2 * dx
L0 -= eta * Dx(r * u[0], 0) * (2 * k[0] + r * Dx(k[0], 0)) * dx
L0 -= eta * Dx(u[0], 1) * Dx(k[0] * r**2, 1) * dx

# z - component:
L1 = -Dx(p, 1) * r * k[1] * dx
L1 -= eta * r * Dx(u[1], 0) * Dx(k[1], 0) * dx
L1 -= eta * Dx(u[1], 1) * Dx(k[1] * r, 1) * dx

# continuity equation:
L2 = Dx(r * u[0], 0) * l * dx
L2 += Dx(u[1], 1) * l * r * dx
L = L0 + L1 + L2

# Coupling terms:
L += mu / (Cn * Ca) * Dx(phi, 0) * k[0] * r**2 * dx
L += mu / (Cn * Ca) * Dx(phi, 1) * k[1] * r * dx
SL = L

# Cahn-Hillard:
```

```
L = (phi - phi0) * q * r * dx
L += Dt * u[0] * Dx(phi, 0) * q * r * dx
L += Dt * u[1] * Dx(phi, 1) * q * r * dx
L += Dt * 1 / Pe * r * Dx(mu, 0) * Dx(q, 0) * dx
L += Dt * 1 / Pe * Dx(mu, 1) * r * Dx(q, 1) * dx
L += Dt * mu * v * r * dx
L -= Dt * dPsidphi * v * r * dx
L -= Dt * Cn**2 * r * Dx(phi, 0) * Dx(v, 0) * dx
L -= Dt * Cn**2 * Dx(phi, 1) * r * Dx(v, 1) * dx
# Contact angle boundary condition:
L -= Dt * Cn * cos(theta1) * v * r * dgdphi * ds(2)
CHL = L
```

The equations are solved using the solve command as shown below.

```
solve(CHL == 0, CHsol,
      solver_parameters={"newton_solver":
       {"linear_solver": "mumps"}})

solve(SL == 0, Ssol, BCs,
      solver_parameters={"newton_solver":
       {"linear_solver": "mumps"}})
```

3.3 Mesh

When solving the CH equation numerically, a high resolution on the mesh is needed. Too low mesh resolution at the interface generally leads to parasitic velocities that grow over time, which causes the interface to deform in a way we do not want. For a given Ca there is an approximate number of grid points required across the interface in order to prevent the instability, typically between five and 15. Using narrower interface means the required number of nodes in the system increases. So in order to have the interface as thin as practically possible, we refine the mesh around the interface.

To refine the mesh on the interface, we identify the points that are within $1 \cdot Cn$ of the interface, and refine the grid around these points. Typically we do the refinement three times, which makes the resolution close to the interface around six times higher than in the bulk, an example of a drop where the mesh is refined on the interface is shown in Figure 3.1.

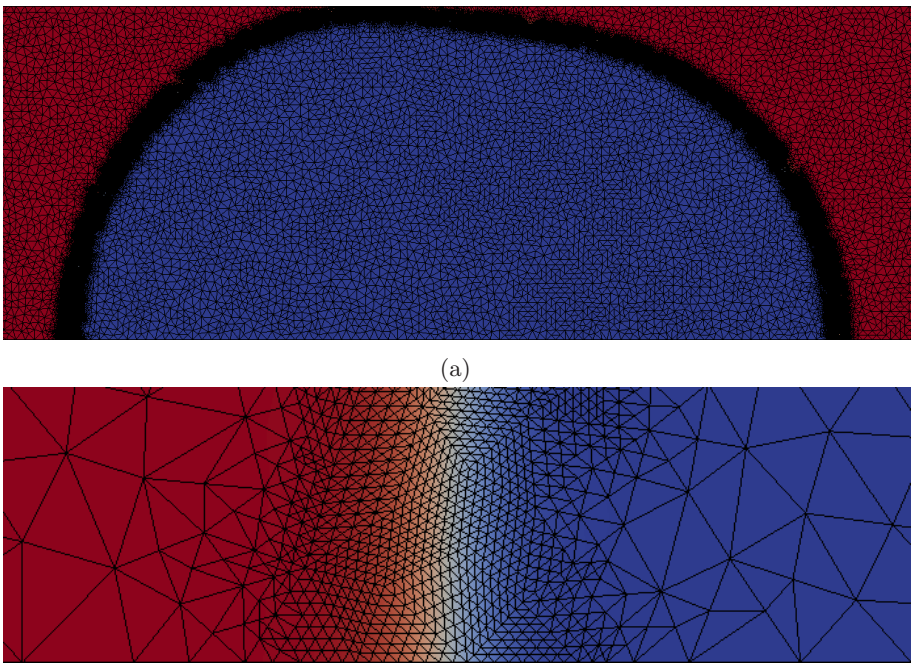

(a)

(b)

Figure 3.1: An example which illustrates the mesh refinement close to the interface and how it relates to ϕ. The color is blue when $\phi = -1$ and red when $\phi = 1$. The black lines show the grid drawn on top of ϕ. (a) shows a drop where the mesh is refined around the interface, and in (b) the bottom left part of the interface is zoomed in on.

CHAPTER 4

Numerical validation

Before we start using the program to study drops in constrictions, we do a series of tests where the numerical results are compared with analytical solutions or published experimental or numerical results in order to validate the code. We begin by first validating the Stokes solver in isolation by looking at pressure driven pipe flow. Then we see if the solver correctly predicts the pressure differential for a drop in equilibrium. Next we consider three transient test cases. The first is the spreading of a viscous drop on a surface and the second the relaxation of a slightly deformed drop. As a final test we look at the shape of a drop in pressure driven pipe flow.

4.1 Stokes flow in pressure driven pipe flow

In order to validate our numerical implementation, we first want to confirm that solutions to the Stokes equations are as expected. To ensure that the CH part of our system plays no role, the surface tension terms $f_r = f_z = 0$ in the momentum equation. The concentration is also set to $\phi = 1$ in the entire domain. To validate the implementation of the Stokes equations, we want to check that we recover the theoretical flow velocity in pressure driven flow. The geometry is a straight pipe, which means $r_c = r_s$ and $r_1 = r_2 = 0$ using the terms shown in Figure 1.1. The boundary conditions are, $p = p_o$ at the outlet and $p = p_i$ at the inlet in addition to $\nabla \mathbf{u} \cdot \mathbf{n} = 0$ where $\mathbf{n}$ is the normal vector. On the wall have the no-slip condition $\mathbf{u} = 0$.

The part of the solution we want to compare with the analytical result is the velocity component in the z-direction u_z. The analytical solution is found by solving the z-component of the Stokes equations (2.27) with $f_z = 0$ and $\eta = 1$. Integrating twice with respect to r and considering cases sufficiently far away from inlets and outlets so that $\partial u_z / \partial z = 0$, we get

$$u_z(r) = -\frac{1}{4}\frac{\partial p}{\partial z} r^2 + A \ln r + B,$$

where $A = 0$ because u_z has to be finite at $r = 0$ and $B = \frac{1}{4}\frac{\partial p}{\partial z} r_s^2$ because of the no-slip boundary condition, which results in

$$u_z(r) = \frac{1}{4}\frac{\partial p}{\partial z}\left(r_s^2 - r^2\right). \tag{4.1}$$

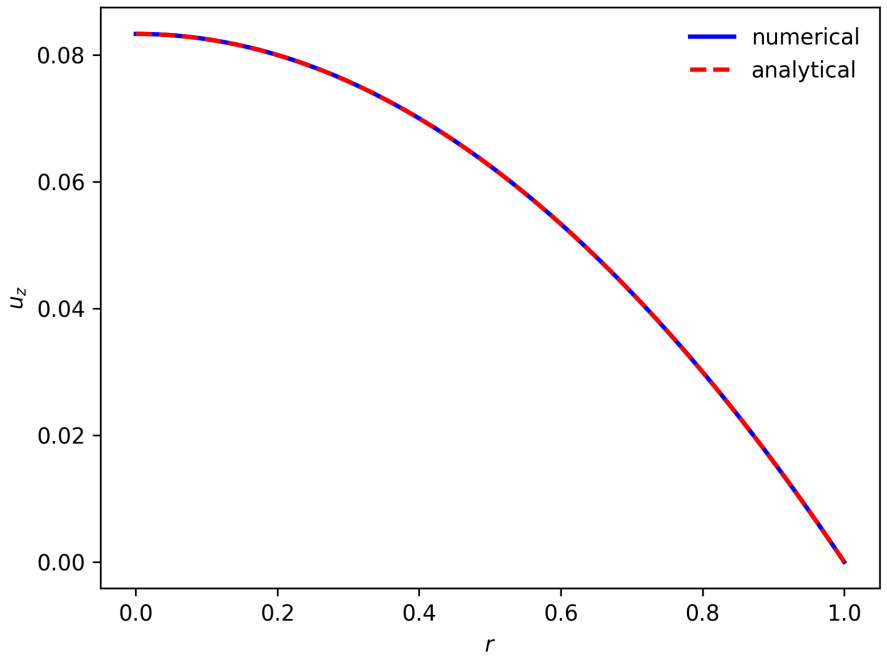

Figure 4.1: The speed parallel to the pipe u_z under constant pressure drop. The solid blue line is the numerical solution extracted from halfway between the inlet and outlet and the dashed red line is the analytical solution given by equation (4.1).

In Figure 4.1 the numerical and analytical solutions are plotted together, and they overlap. The maximum value for the relative error is 0.02% with 100 elements in the radial direction.

4.2 Laplace pressure jump

The second test, is to consider the pressure jump across the interface of a drop in equilibrium. At equilibrium the sum of forces that act on the interface must equal to zero for all parts of the interface. Following [43, p. 76-79] we can therefore divide the interface into smaller areas A with C being the boundary curve around the element. The force generated by the stress on the interface element is found by integrating the stress on the element over the area. This must be balanced by the surface tension force, which is found by integrating the surface tension over the boundary curve. So the equilibrium condition is

$$\int\int_A (\mathbf{T} - \hat{\mathbf{T}}) \cdot \mathbf{n} dA + \int_C \sigma \mathbf{t} dl = 0, \tag{4.2}$$

where $\mathbf{T}$ and $\hat{\mathbf{T}}$ is the total bulk stress in the fluid when approaching from the outside and inside respectively, $\mathbf{n}$ is the normal vector pointing out and $\mathbf{t}$ is the normal vector to C which is tangent to A and pointing out. The line integral

Table 4.1: The error in Laplace pressure difference for different resolutions of the interface. The interface thickness given by Cn, number of elements across the interface ε/h and the pressure error in percent $\Delta p_{error}(\%)$.

Cn	ε/h	$\Delta p_{error}(\%)$
0.01	10	2.25
0.01	12	0.95
0.01	14	0.51

can be written as a surface integral with Stokes' theorem

$$\int_C \sigma \mathbf{t} dl = \int \int_A \left[\nabla\sigma - \mathbf{n}(\mathbf{n}\cdot\nabla)\sigma - \sigma\mathbf{n}(\nabla\cdot\mathbf{n})\right] dA. \tag{4.3}$$

Since the force equilibrium (4.2) must be valid for any chosen surface element on the interface, the integrands must also sum to zero

$$(\mathbf{T} - \hat{\mathbf{T}})\cdot\mathbf{n} + \nabla\sigma - \mathbf{n}(\mathbf{n}\cdot\nabla)\sigma - \sigma\mathbf{n}(\nabla\cdot\mathbf{n}) = 0. \tag{4.4}$$

We find the normal stress balance by multiplying eq. (4.4) with the normal vector $\mathbf{n}$. Since we are looking at a drop in equilibrium, the velocities are zero and the total bulk stresses are simplified to $\mathbf{T} = p\mathbf{I}$ and $\hat{\mathbf{T}} = \hat{p}\mathbf{I}$ where $\hat{p}$ and p are the pressures on the inside and outside of the drop. Additionally our surface tension is constant and for a sphere $\nabla\cdot\mathbf{n} = 2/R$ with R being the radius of the sphere. This gives us the pressure differential for a spherical drop

$$\hat{p}_{tot} - p_{tot} = \frac{2\sigma}{R}. \tag{4.5}$$

In order to compare with numerical results we make eq. (4.5) dimensionless by dividing both sides with the characteristic pressure $\eta U/L$, which results in the non dimensional pressure difference

$$\Delta p = \frac{4\sqrt{2}}{3}\frac{1}{Ca}. \tag{4.6}$$

To see if we find the same pressure difference, a drop is initialized using the equilibrium solution in one dimension (2.13) with x replaced by r. The drop is given a radius of $r_1 = 1$ with a center in origo and the domain is a rectangle from 0 to 5 in the r-direction and -5 to 5 in the z-direction. On the boundaries we set $p = 0$ and $\nabla\mathbf{u}\cdot\mathbf{n} = 0$ for the Stokes equations. For the CH equation we use the Neuman condition on the chemical potential and set $\theta_c = 0$ in equation 2.15. The equilibrium drop profile ends up being very similar to the analytical one dimensional solution, see Figure 2.2. For $Ca = 1$, the results for the error in pressure $\Delta p_{error}(\%)$ and how it changes with the number of elements across the interface for $Cn = 0.01$ are summarized in Table 4.1. With 14 elements across the interface we get an error of 0.51% for $Cn = 0.01$.

4.3 Drop spreading case

Since the two prior validation cases have been at equilibrium or stationary, we have not yet verified that the solver works on transient problems. To achieve

this, we consider the spreading of a viscous drop on a surface. The spreading process can be divided into two parts. In the beginning the spreading is similar to coalescence of two spherical drops, and Stokes flow calculations on high viscosity drop coalescence shows that the radius of the wetted area R follows a log-law [19]

$$R = -at \ln R, \tag{4.7}$$

where a is an adjustable parameter and t is the non-dimensional time which has been scaled with the characteristic time $4\pi\eta R_0/\sigma$ where R_0 is the initial radius of the drop.

In the later stage for small contact angles θ_m, the drop is shaped as a spherical cap in the region far away from the contact line, also known as the outer region

$$\frac{dh_o(x)}{dx} = \frac{2V}{\pi r_1^2}\left[\frac{2}{r_1} - \frac{2r}{r_1^2}\right], \tag{4.8}$$

where V is the drop volume, $h_0(x)$ is the interface height in the outer region and r_1 is the drop radius. Close to the contact line, the thin film equation can be used to described the interface profile $h(x)$ [66]

$$\frac{d^3h(x)}{dx^3} = -\frac{3Ca}{h(x)^2}. \tag{4.9}$$

For a vanishing slope at infinity equation (4.9) can be solved with [22]

$$\left(\frac{dh(x)}{dx}\right)^3 = \theta_m^3 + 9Ca \ln\left(\frac{x}{l_m}\right), \tag{4.10}$$

where l_m is the slip length and θ_m is the contact angle at equilibrium. Imposing that $\theta_m = 0$ the solution in the contact line region can be matched with the outer solution which results in Tanner's law

$$R \sim t^{1/10}. \tag{4.11}$$

The spreading is simulated by placing a spherical drop which is 50 times more viscous than the surrounding liquid on top of a surface with a no-slip boundary condition. The mesh has a triangular shape, and on the remaining boundary, we allow $\mathbf{u} \neq 0$ and set the pressure to be constant $p = 0$, shown in Figure 4.2. We expect the capillary numbers to be of order ~ 0.01, so to get the contact line speed close to 1 we set $Ca = 0.01$ for the simulations. With $Cn = 0.01$ we run simulations of drops with contact angles $\theta_c = 10°, 15°, 30°$ and for $Cn = 0.005$ with $\theta_c = 30°$. The evolution of the interface over time is shown in Figure 4.2 for $\theta_c = 10°$ and $Cn = 0.01$. To compare our results with the log-law (4.7) and experiments from [19] we scale the time by multiplying with 0.01 since we set $Ca = 0.01$ in the simulations and also take into account the 4π factor used in equation (4.7) to scale the time. Using the fitting parameter $a = 9$ for the numerical simulations we plot our results together with the log-law (4.7) and experimental results on drops with equilibrium contact angles $\theta_{eq} \approx 0°, 85°$ from Eddi et al. [19] in Figure 4.3. In the initial phase of the spreading the numerical results are different from the experiments and do not follow the drop coalescence solution. The are a couple of reasons for this. The first is that the boundary condition for ϕ does not allow non-equilibrium contact angles

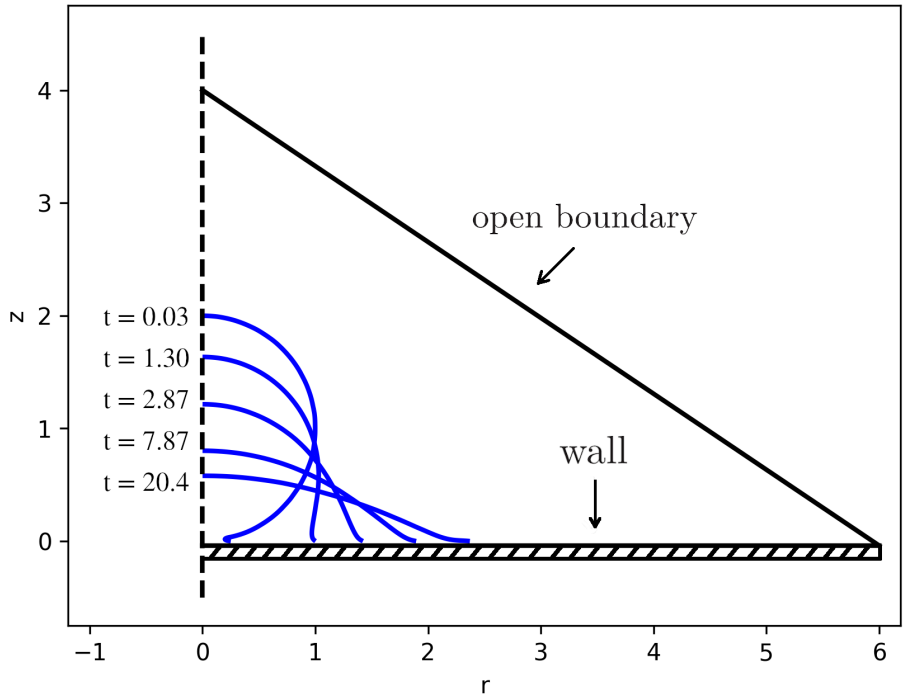

Figure 4.2: Spreading of droplet with contact angle $\theta = 10°$. The profile of the interface is shown at $t = 0.03, 1.30, 2.87, 7.87, 20.4$. The triangle shaped domain is marked with lines, and the symmetry axis is marked with a dashed line at $r = 0$. We use $Cn = 0.01$ and $p = 0$ on the open boundary and $\mathbf{u} = 0$ on the wall.

which is needed to accurately simulate this phase of the spreading [9]. We also notice that the drop with $Cn = 0.005$ spreads slightly slower in the initial phase compared to the three drops with $Cn = 0.01$ and it starts following the log-law earlier. At about $t = 0.03$ the drops with $Cn = 0.01$ and $Cn = 0.005$ with the same contact angle show the same wetting radius and continue to do so as the drop spreads further. When the initial phase of the spreading is done, the numerical results are in good agreement with the experimental data from Eddi et al. [19].

We had also hoped that the case with $\theta_c = 10°$ would follow Tanner's law in the later stage of spreading. However after the drop was allowed to spread for a long while a large area of the surface the drop is spreading on has $|\phi| < 0.9$ and the results appear non-physical.

4.4 Relaxation of drop

Next we perform another test on a dynamic problem to confirm the validity of our code. We look at the retraction of an ellipsoidal droplet back to spherical shape. How the drop changes shape as a function of time can be found for small deviations from spherical shape and low capillary numbers. To describe a drop

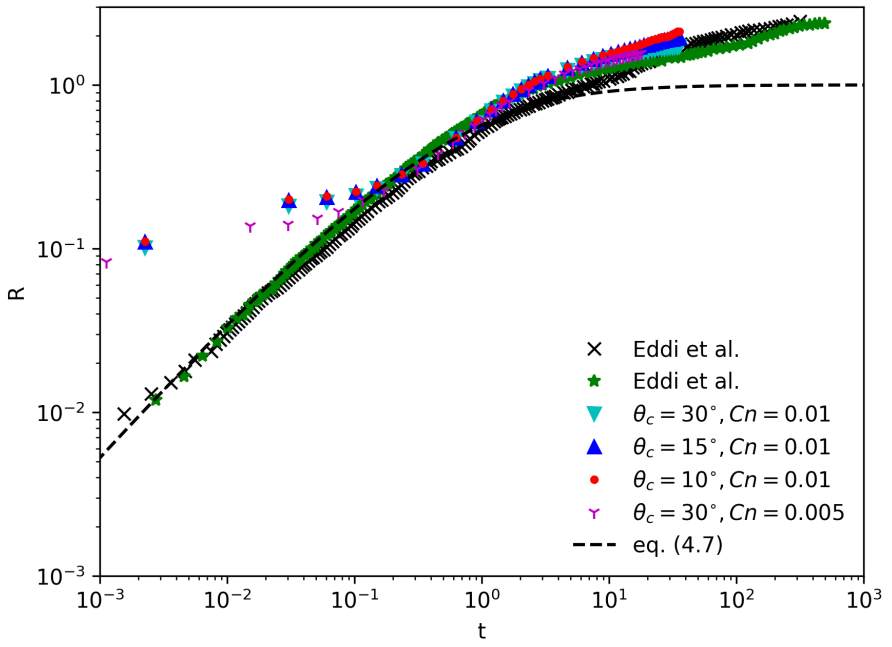

Figure 4.3: Results of spreading of a viscous droplet on a surface with contact angles $\theta_c = 30°, 15°, 10°$ and $Cn = 0.01$ and one case with $\theta_c = 30°$ and $Cn = 0.005$. The dashed line is the log-law theory as given by equation (4.7) using $a = 9$ as the fitting parameter.

surface slightly distorted from a sphere [60] suggested using

$$(\mathbf{x} + \mathbf{x})^{(1/2)} = 1 + \alpha \mathbf{x} \cdot \mathbf{A} \cdot \mathbf{x} + \mathscr{O}(\alpha^2) \qquad \alpha \ll 1,$$

where $\mathbf{A}$ is the distortion from a spherical shape and $\mathbf{x}$ is the position vector relative to the center of mass of the drop. With the time evolution of $\mathbf{A}$ being [60]

$$\alpha \frac{\partial \mathbf{A}}{\partial t} - \alpha \hat{Ca} \omega \cdot \mathbf{A} + \alpha \hat{Ca} \mathbf{A} \cdot \omega = \frac{5 \hat{Ca} \mathbf{e}}{2\eta + 3} - \frac{40(\eta + 1)\alpha \mathbf{A}}{(2\eta + 3)(19\eta + 16)} + \mathscr{O}(\alpha \hat{Ca}, \alpha^2),$$

where ω, $\mathbf{e}$ are the vorticity and strain tensors, $\eta = \eta_d / \eta_c$ where η_d and η_c are the viscosities of the dispersed and continuous phases respectively, $\hat{Ca} = \eta_c \dot{\gamma} L / \sigma$ with $\dot{\gamma}$ being the shear rate and t is the time scaled with $\sigma / (\eta_c L)$. Since we are looking at the relaxation of droplet there is no applied flow field [27] so $\mathbf{e}$ and ω can be neglected. Additionally if $Ca \ll 1$ it simplifies to

$$\frac{\partial \mathbf{A}}{\partial t} = -\frac{40(\eta + 1)\mathbf{A}}{(2\eta + 3)(19\eta + 16)},$$

which can be solved for $\mathbf{A}$ as an exponential decay. Solving the preceding ordinary differential equation leads to the following expression for the deformation over time

$$D(t) = D_0 \exp\left(-\frac{40(\eta + 1)}{(2\eta + 3)(19\eta + 16)} \frac{t}{Ca} \right), \tag{4.12}$$

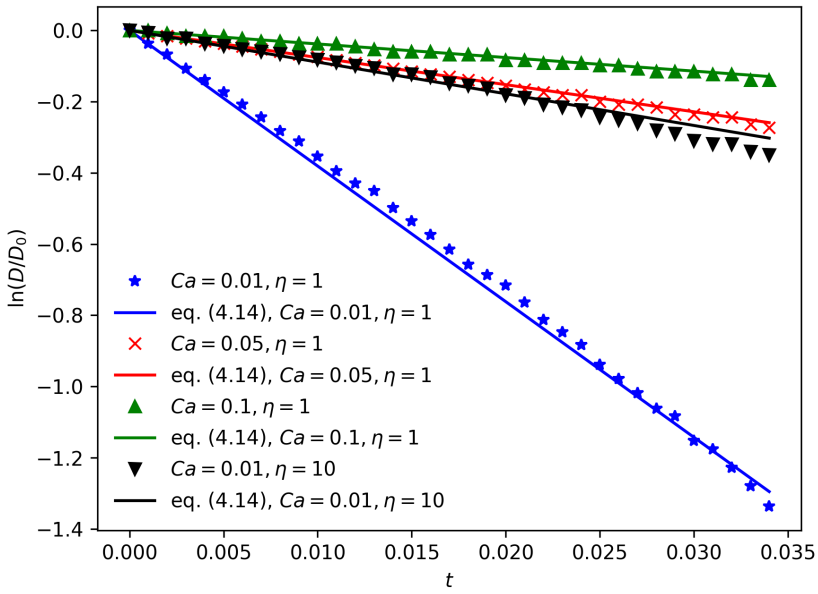

Figure 4.4: Comparison of numerical results for $Ca = 0.01$ with $\eta = 1, 10$ and $Ca = 0.05, 0.1$ for $\eta = 1$, with $Cn = 0.01$. The markers are the numerical results and the line are the respective analytical solution.

where we have changed back to the definition of Ca and dimensionless time t given by (2.19). D is the Taylor deformation parameter given by the following equation

$$D = \frac{a - b}{a + b} \tag{4.13}$$

where a and b are major and minor axes of the drop. By dividing by D_0 and taking the natural logarithm, equation (4.12) can be written as

$$\ln\left(\frac{D(t)}{D_0}\right) = -\frac{40(\eta + 1)}{(2\eta + 3)(19\eta + 16)} \frac{t}{Ca}. \tag{4.14}$$

The simulations are initialized with $a = 1.25$ and $b = 0.83$ and the drop as allowed to relax. To prevent the initial shift in the bulk of ϕ to affect the results, we start measuring the deformation after a few timesteps, when $D_0 = 0.11$. The drop is in a rectangular domain with r from 0 to 5 and z from -5 to 5. On the boundaries of the domain, $p = 0$ and $\nabla \mathbf{u} \cdot \mathbf{n} = 0$. The usual boundary conditions for μ and ϕ apply with $\theta_c = 0°$. In Figure 4.4 the numerical results for $\ln(D(t)/D_0)$ for $Ca = 0.01, 0.05, 0.1$ with $\eta = 1$ and $Ca = 0.01$ with $\eta = 10$ is plotted together with the analytical solutions. The numerical and analytical solutions are in good agreement.

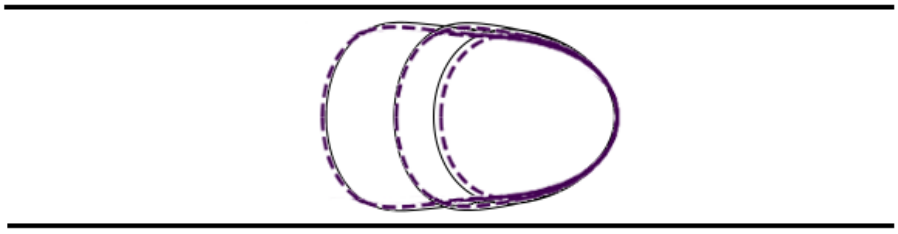

Figure 4.5: Drop profile in pressure driven pipe flow. The dashed lines are our numerical results for three drop volumes. The straight lines are numerical results from [42]. The capillary number is $Ca = 0.05$, the viscosity ratio is $\eta = 10$ and the interface thickness is given by $Cn = 0.01$.

4.5 Drop shape in a pipe

As a final validation test we consider a case similar to drop squeezing through constrictions. We want to check that the shape of a simple drop in pressure driven flow in a straight pipe is in agreement with other numerical results.

We place a simple drop inside a straight pipe, $r_c = r_s$ and $r_2 = 0$ using the terms from Figure 1.1. The boundary conditions with respect to p and $\mathbf{u}$ are $p = p_i$ at the inlet, $p = p_0$ at the outlet with $\nabla\mathbf{u} \cdot \mathbf{n}$ at outlet and inlet. We follow the perspective of the drop by setting the velocity on the wall to be the desired drop velocity $\mathbf{u} = -\mathbf{i}_z$, where $\mathbf{i}_z$ is the unit vector in the z direction. The pressure drop is set in such a way that the drop does not move in the z direction. When the drop has taken on a steady shape, we extract the drop profile. For this test we set $Ca = 0.05$ and $\eta = 10$. Because some have radius bigger than the pipe, the drops are initialized with a cylindrical shape with the same volume as the undeformed drop.

With simulations using the boundary integral method Lac and Sherwood [42] found the shape of drops in pressure driven pipe flow at $Re \ll 1$ with $\eta = 0.1, 1, 10$ and $Ca = 0.05$. In Figure 4.5 we plot Lac and Sherwood and our results for three drop volumes. There is a small difference in drop volume which comes from the shift in ϕ values as the drop is initialized, but the results are in good agreement.

CHAPTER 5

Experimental method

In addition to exploring the squeezing of drops through constrictions using numerical simulations, we also take an experimental approach. The experiments were done during a three month stay in Paris at École supérieure de physique et de chimie industrielles de la Ville de Paris (ESPCI) and Institut Pierre-Gilles de Gennes pour la Microfluidique (IPGG). The experimental setup can be divided in two parts. The generation of drops using microfluidic techniques and polydimethylsiloxane (PDMS) chip manufacturing, and the second part which is to push these drops through a constriction.

5.1 Generation of simple drops

Drop generation in microfluidics can be divided into passive and active methods [26, 47, 69, 85]. In passive methods the dispersed (drop) fluid is introduced to the continuous (outer) fluid, and drops are generated from the interaction between the two fluids. The active methods have an additional level of control, for example by adding an external electric or magnetic field or by varying the flow rates or material properties. The active methods give more control and are suitable when a great variety of drop configurations are needed. In this project, only passive droplet generation methods were used.

The passive methods can be separated into three categories: co-flowing, flow focusing and cross-flowing designs. We opt for the flow focusing design because it is well suited for planar microfluidic chips. In the flow focusing method [6, 26, 47, 71, 73, 85], illustrated in Figure 5.1 the dispersed fluid is introduced from the right and the continuous fluid comes from the top and bottom channels. The two fluids meet where the channels intersect and drops are formed. The PDMS chip shown in Figure 5.1 was fabricated at IPGG and a description of that process is given in the next section.

In all three passive methods, droplets can be generated in the squeezing, dripping and jetting regimes, which are mostly determined by the flow rate ratio and capillary number [26, 85]. In the squeezing regime, typically at $Ca < \mathcal{O}(10^{-2})$ the dispersed phase is pushed into the intersection, and as it begins to increasingly prevent the flow of the continuous phase, the outer phase pinches off the neck close to the dispersed phase channel end, this regime is shown in Figure 5.1. Within this regime, the droplets can have a length of several channel widths. If the dispersed phase flow rate is kept constant, increasing the flow rate of the continuous phase will reduce the droplet size and

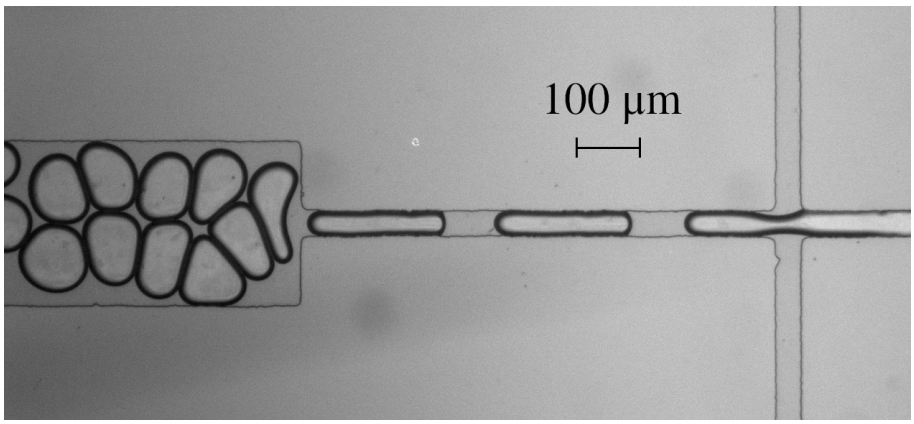

Figure 5.1: A PDMS chip with 50 μm wide channels with a flow focusing design for drop generation. In this image, drops are generated in the squeezing regime. The dispersed water phase is pushed in from the right, and the continuous oil phase comes from the top and bottom.

vice versa. Increasing the continuous flow rate and thus the capillary number further, a transition to the dripping regime eventually occurs. In the dripping regime viscous forces are more important, and so the interface is ruptured because of drag between the continuous phase and the dispersed phase. In this regime, the drops are about the size of the channel or smaller. The jetting regime is distinct from the other two in that the pinch-off does not occur in the intersection but instead after it. A jet of the dispersed liquid extends further beyond the end of the dispersed channel than in the other regimes, and the pinch-off happens near the end of the jet, typically outside of the intersection. In this regime, drops are larger and less uniform than in the dripping regime. The jet remains extended out of the dispersed channel after a droplet is released, unlike for squeezing and dripping where the interface is drawn back into the dispersed channel after release.

In order to have stable drops, surfactants are often used to reduce surface tension on the interface [26]. Surfactants have one hydrophobic and one hydrophilic part and can be added to one of the phases. When the dispersed and continuous phases come into contact, the surfactants migrate towards the interface and reduce the surface tension and increase drop stability. Surfactants can typically reduce the surface tension by up to a factor of ten [26]. The timescale for the migration of surfactants to the interface is about the same as for droplet generation [26], so determining the capillary number during droplet generation can be challenging. However, since our focus is not to understand the drop generation process, but instead drop dynamics at a much later time we can assume that the surface tension does not depend on time.

5.2 PDMS chip fabrication

The flow focusing design and the drop generation is implemented using PDMS chips, which is the standard in microfluidics [69]. The PDMS used was Sylgard 184 from Dow Corning. The chip manufacturing process consists of the following

steps. First we make a design for the flow focusing setup using CAD, in this case Autodesk Inventor. The design has several copies of the same design, which allows us to create several chips at once. The pattern is then automilled which results in a wafer that can be reused many times. PDMS is mixed with a $10:1$ mixing ratio of base to crosslinker, and poured onto the wafer. The mixed PDMS has a lot of air bubbles, so it is placed in a vacuum chamber for several hours to remove the bubbles. After the air bubbles have been removed the PDMS and wafer are put into an oven at 70°C for a few hours to cure the PDMS. After the PDMS has cured it is peeled from the wafer, and using a razor the PDMS is separated into pieces, one for each design. The resulting PDMS pieces have the flow focusing channels on the bottom.

Holes for inlets and outlet are made with a PDMS puncher (1 mm diameter for the inlets, and 2 mm for the outlet) by pushing through the PDMS from the top, through the PDMS and into the inputs and output. The side of the PDMS chips that has the flow focusing channels, inputs and output is still open to air and needs to be sealed. Before sealing the last side, a capillary is pushed through the outlet several times in order to reduce the chance of PDMS dislodging from the chip, when the constricted capillary is connected with the chip. If we do not want to seal the chips up right away, the open side of the chips are covered with scotch tape to prevent dirt from entering the channels.

In order to seal the last side of the chip, a glass slide is bonded to the chip using plasma bonding. The glass slide, and the chip with the bonding side facing up, is put in a plasma cleaner where the surface properties of the glass and PDMS are altered. After the plasma cleaning, the bonding side of the chip is put into contact with the glass slide. The slide and PDMS bond together sealing the channel side of the chip. The plasma cleaning process makes the inside of the chip hydrophilic and it will gradually turn hydrophobic over many hours. To hasten the process the chip can be placed inside an oven at 90°C to make the chip hydrophobic within a few hours.

5.3 Liquid properties

The liquids we use in the experiments are water as the dispersed phase, and sunflower oil with 5% of the surfactant polyglycerol polyricinoleate (PGPR) as the continuous phase. For the dynamic viscosity of water we use $\eta_w = 1.00$ mPa·s which is the value for water at 20°. For the sunflower oil solution, we measured the viscosity by using a Mocular Compact Rheometer (Anton Paar MCR 302) to measure the torque required to turn an object submerged in the solution. The measurements, which are shown in Figure 5.2, result in a dynamic viscosity of $\eta_s = 82.4 \pm 0.3$ mPa·s, where the uncertainty is defined as one standard deviation. Based on these viscosity measurements, the expected viscosity ratio for the two liquids is then $\eta = 82.4^{-1}$.

The surface tension was measured using a tensiometer (Krüss DSA30) which uses the pendant drop method [17]. The surface tension was measured after $10, 20$ and 50 seconds, and is shown in Figure 5.3 for both solutions and summarized in Table 5.1. It is clear that the surfactant reduces the surface tension with an order of magnitude.

To check if our measurements of surface tension are reasonable we compare with [56], where they found pure sunflower oil/water surface tension to $\sigma_{pure} =$

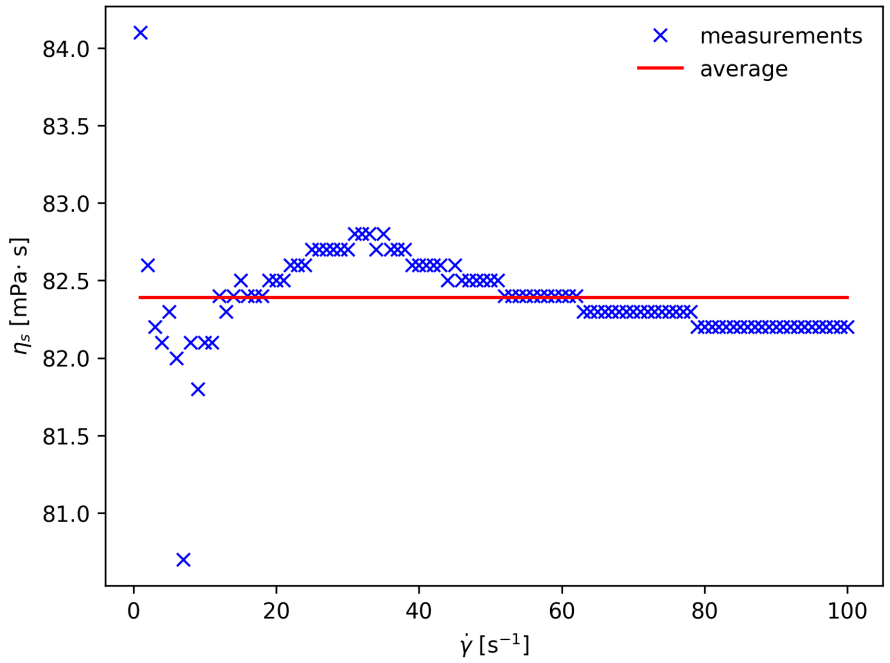

Figure 5.2: Viscosity of sunflower oil with PGPR η_s measured at different shear rates $\dot{\gamma}$. The line shows the average viscosity measured.

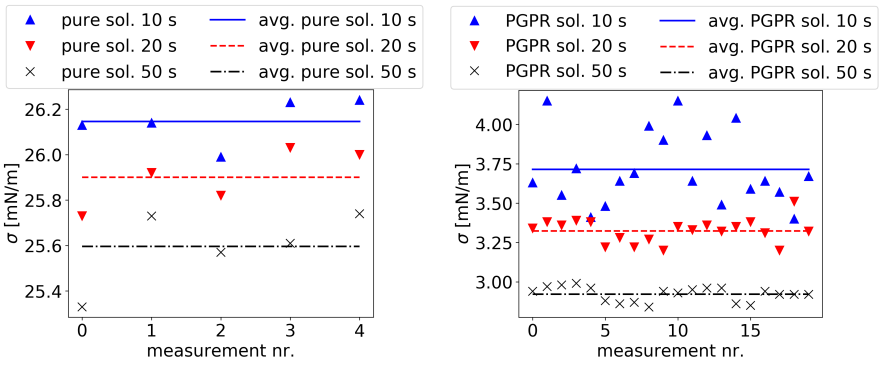

(a) (b)

Figure 5.3: Surface tension measurements σ with the pendant drop method of pure sunflower solution (a) and the sunflower with PGPR solution (b) after allowing $10, 20$ and 50 s for equilibriation. The lines show the average surface tensions measured.

Table 5.1: Measurements of surface tension σ using the pendant drop method of water in sunflower oil with and without the surfactant after allowing $10, 20$ and 50 s for equilibriation.

σ [mN/m] surfactant			σ [mN/m] pure		
10 s	20 s	50 s	10 s	20 s	50 s
3.7 ± 0.3	3.32 ± 0.07	2.92 ± 0.05	26.1 ± 0.1	25.9 ± 0.1	25.6 ± 0.1

27.5 ± 0.3 mN/m, and sunflower oil with 5% PGPR to have a surface tension to water of $\sigma_{NIS16} = 3.03 \pm 0.05$ mN/m when measuring after allowing the surface to equilibriate for 10 minutes, which is in reasonable agreement with our measurements, given that it is sunflower oil we are using where some variability in its properties are to be expected.

5.4 Capillaries with constriction

To make a geometry similar to what is shown in Figure 1.1, we use glass capillaries. The capillaries chosen for the experiments with single emulsions have a length of 10 cm. Since the numerical model is based on $Re \ll 1$, we need the Reynolds number to be very small in the experiments. One way to ensure $Re \ll 1$ is to use capillaries with very low radii, but for smaller radii the capillaries become more fragile especially around the constriction. So glass capillaries with inner radius $r_s = 0.58$ mm are chosen because they are small enough to have viscous forces dominate over inertia given low enough flow rates, but also big enough that if handled very carefully they do not break. In order to make a constriction on these capillaries, a pipette puller (Narishige PN-31) is used. As shown in Figure 5.4, the capillary is inserted into two platinum wires that have been shaped by hand. The capillary is fastened to two mounting points on either side, the platinum wires are then heated by passing a current through them as a force gradually pulls the mounting points apart. After a certain period of time, typically 30 s, and due to the incompressibility of the molten glass, a constriction is thus formed by the action of this stretching. The machine is stopped before the capillary is split into two separate pieces, leaving us with a constricted capillary, an example of which is shown in Figure 5.5.

5.5 Experimental setup

An example of a final device is shown in Figure 5.6. For the first steps in building the setup, the channels of the chip and capillary are parallel and perpendicular to the ground respectively (rotated 90° compared to Figure 5.6). Before connecting the capillary to the chip, a tube for the output is connected to the capillary. Prior to pumping any liquid into the chip, the other end of the capillary is pushed into the outlet of the chip and the connection is sealed with epoxy. The continuous phase is then connected to its inlet and is pushed almost all the way to the intersection using a pressure controller (FLUIGENT MFCS-FLEX 4C). The reservoir for the dispersed phase is then connected to the

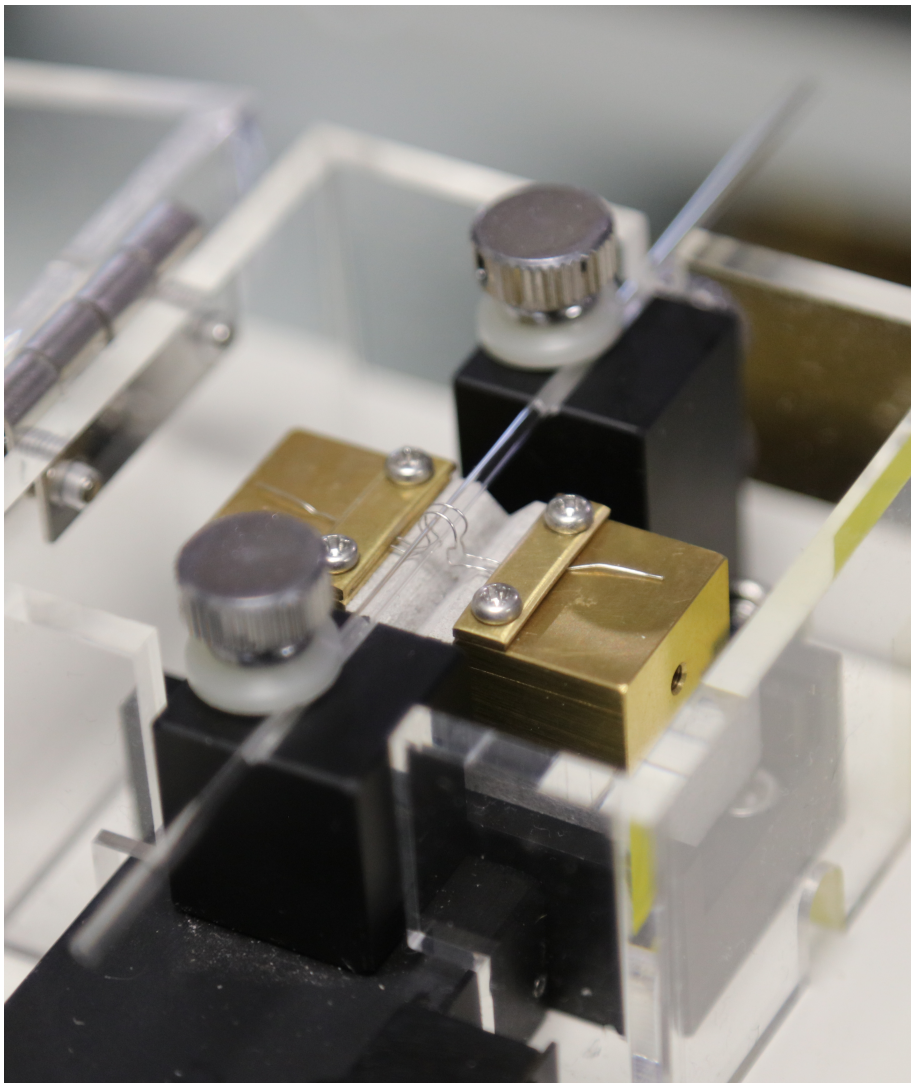

Figure 5.4: A pipette puller, with the capillary inserted into platinum wires. The capillary is attached with retention screws on both sides. The outer diameter of the capillary is 1.5 mm.

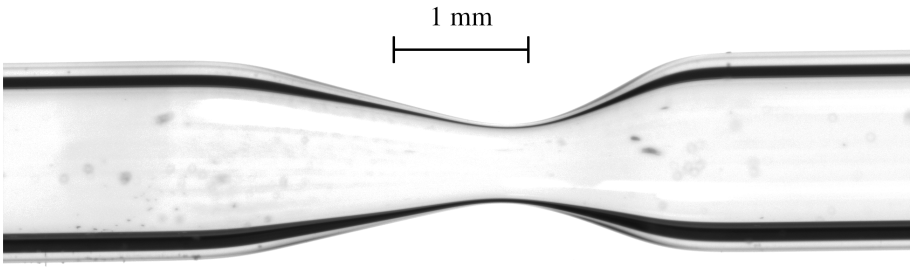

Figure 5.5: An example of a glass capillary with a constriction made using a pipette puller.

inlet and is also pushed to the intersection using the pressure controller. When both liquids have reached the intersection, both liquids are pushed through the chip, and about half-way through capillary, where the pressures are reduced so the liquids remain still.

The device is then rotated 90° to the orientation shown in Figure 5.6 and the constriction is placed on a glass slide with glycerol on it. Glycerol is used because it has refractive index close to glass which reduces optical distortion caused by the transition between the glass and surroundings [14]. More glycerol is then put on top of the constriction and another slide is placed on top, ensuring that the constriction and area around is fully immersed in glycerol (middle of Figure 5.6). A mirror is placed below the constriction redirecting light from a light source so that the light passes vertically through the constriction and another mirror reflects the light horizontally towards a camera.

Since we assume creeping flow in the simulations, we want Re to be sufficiently low in the experiments. For example $Re \sim 0.001$ means we would need drops to move at $U \sim 0.1$ mm/s. At these low flowrates, drops could not be generated. So drops were instead generated at higher pressures (flow rates), and when the capillary was filled with the drops, the pressures were reduced and allowed to stabilize before images were taken.

5.6 Compound drops

To create compound drops, we tried three different approaches. One method was first creating the inner emulsion in a PDMS chip, and storing the output in a reservoir, and then using this output as input for an other PDMS chip with wider channels. The two other methods were based on making one single device that creates the compound drop in either one step or two. For surfactants we also tried adding the surfactant sodium dodecyl sulfate (SDS) in the water phase.

In the two-step method, we first created the inner droplet with diameters about ~ 500 μm. It was soon observed that the stability of these droplets was not sufficient. When the droplets reached the output container, they would break up into smaller drops with diameters about 10 μm within 30 minutes, which was considerably smaller than the constriction diameter making them too small for our use.

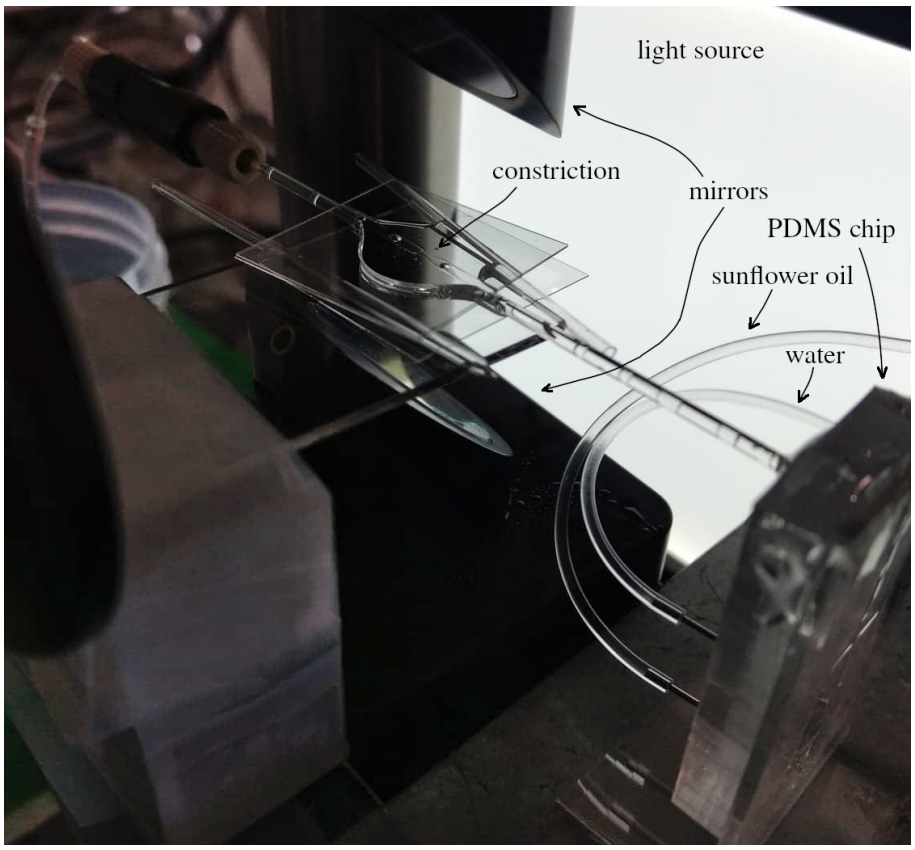

Figure 5.6: Setup for simple drops pushed through a constriction. In the bottom right corner, a PDMS chip with inlet tubes for oil and water are connected on the lower part, and the capillary with outer diameter of 1.5 mm is connected to the top part. In the middle of the image, the constricted part of the capillary is placed between two glass slides, with two mirrors for redirecting light from the light source, through the device and into the camera lens.

The first type of one-step device we assembled and used has two circular capillaries inside of a square capillary as shown in Figure 5.7, this type of device has been commonly used to make compound drops and capsules [55, 72]. An image of one of the devices we made is in Figure 5.8. The tips for the circular capillaries, were made by first pulling a capillary with a pipette puller, a microforge was then used to make the tips as flat as possible and with the appropriate diameter. When they were inserted into the square capillary, they were aligned such they their axes of symmetry were as close the the middle of the square capillary as possible. A close up of the tips in Figure 5.8 is shown in Figure 5.9, where we see that the tips are not completely flat, but they are aligned well. Four of these devices were created, as the first devices were not properly alligned, or the tips not sufficiently flat. The last and most succesfull iteration, was an o/w/o configuration with the output capillary treated to be hydrophobic, by immersing it in hexane, chloroform and octadecyltrichlorosilane (OTS) at 200°C for more than 5 hours. After working with these devices, we

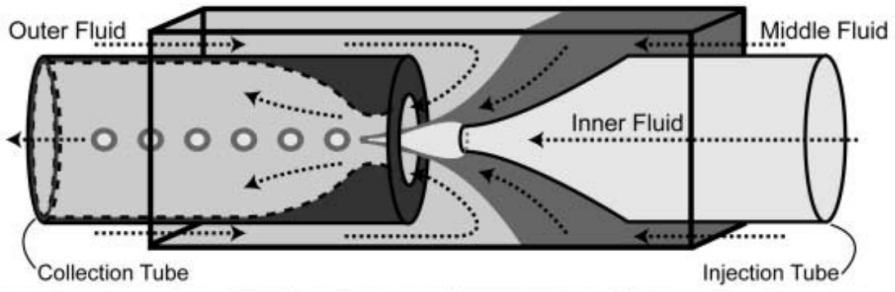

Figure 5.7: Illustration of one-step compound drop device, with two circular capillaries inside of a square capillary reproduced from [72].

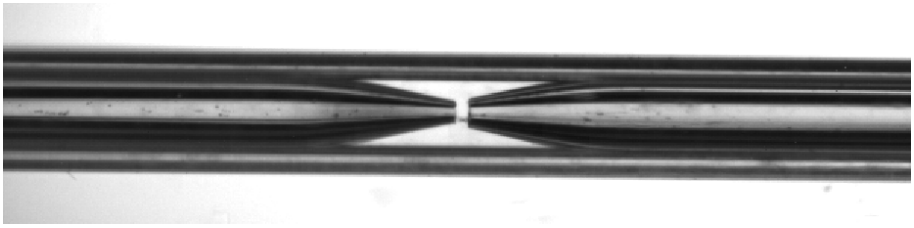

Figure 5.8: A one-step compound drop device, with two circular capillaries inside of a square capillary. The outer diameter of the square capillary is 1.5 mm.

speculated that also for this method, the droplet size was a major factor in the difficulty in reliably creating compound droplets. With the same geometry [73] reports that this method can be used to create compound drops with diameter up to 1 mm, so this flow-focusing method itself is not the limitation. One difficulty that we observed when creating these devices was that the difficulty of creating flat tip-endings for the round capillaries increased with size. If we had found another method of making the tips smooth and flat we could most likely have made this method work.

The third method was to connect two PDMS chips with different channel widths together. This setup showed more promising results than the previously discussed device. Since the outer phase was oil in one chip and water in the other, the chips had to be hydrophobic and hydrophilic respectively. This meant that device would be useful for a few hours before the hydrophilic chip gradually turned hydrophobic. The output of the first chip was connected to the inner phase input of the second one. In the output of the second chip, the constricted capillary was attached in the same way as for the single emulsion setup. For this setup each component of the device worked as intended. We were able to make the internal droplet and they would transfer into the second chip. Additionally we were able to make the outer droplet in the second chip and send them through the constriction. Unfortunately making these two processes happen at the same time was very difficult. To create the inner droplets, the input pressures had to be such that the liquid from the first chip could freely flow into the second chip. When the input pressure for the secondary chip was increased, the flow rate was reduced in the first chip, and the production of

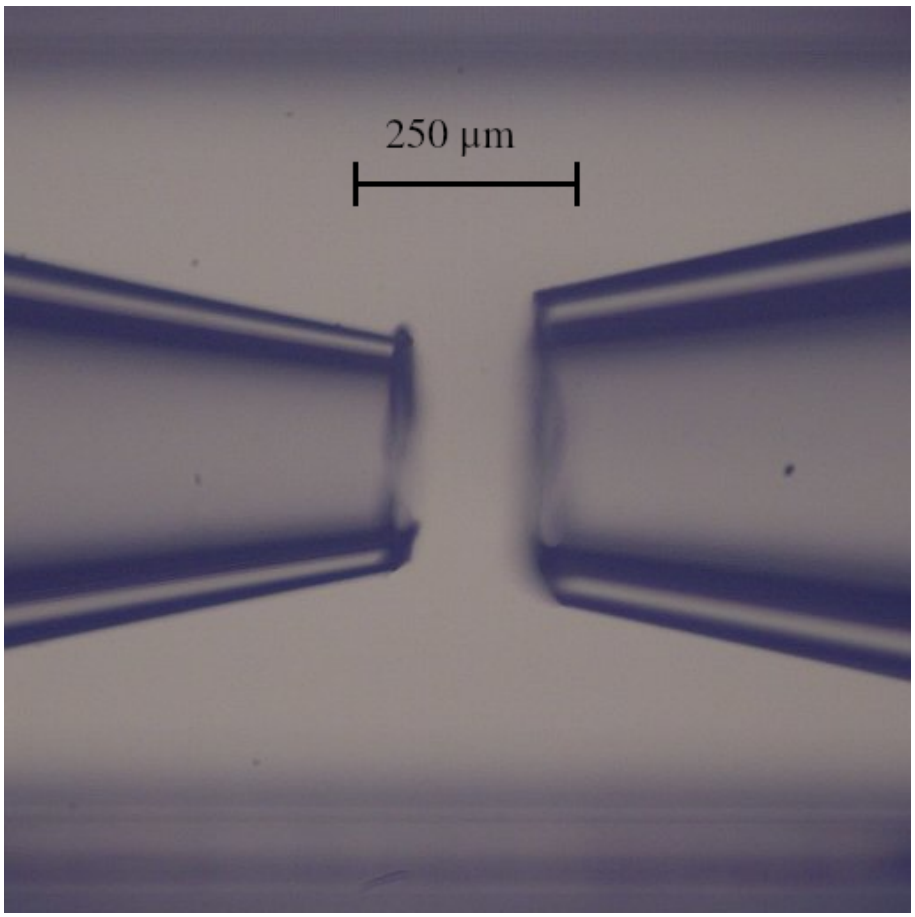

Figure 5.9: A close-up of the tips of the circular capillaries in the one-step compound drop device shown in Figure 5.8.

droplets seized. Trying many input pressure combinations, a few compound drops were created, see Figure 5.10. It is conceivable that if we controlled the flow rates directly instead of the pressure, we would be able to solve this issue, but we did not have time to try this. We have not been able to find this setup in the literature to see how others have controlled this type of device.

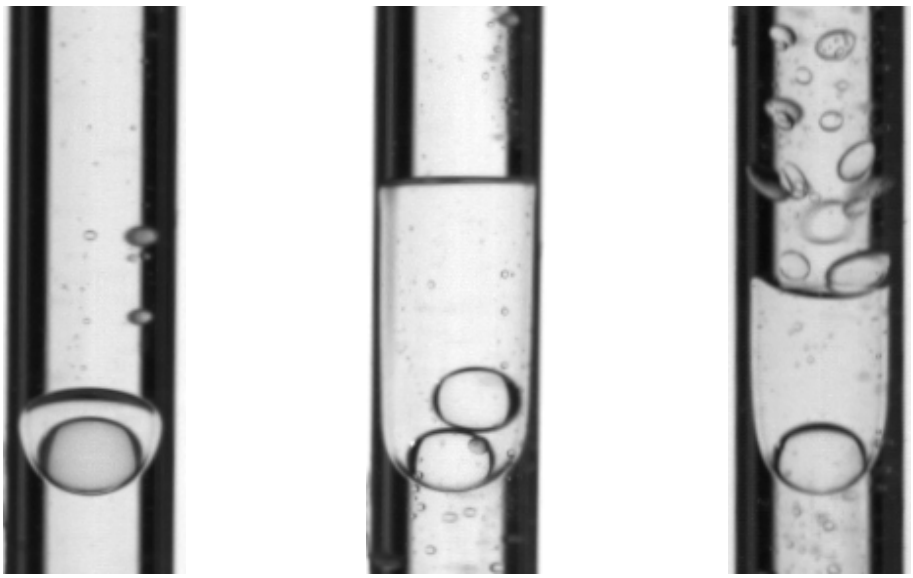

Figure 5.10: Examples of some compound drops that were created using the two-PDMS chips setup. The outer phase is sunflower oil with 5% PGPR, middle phase is water with 1.9 g/L SDS and inner phase is sunflower oil. The outer diameter of the capillaries are 1.5 mm.

CHAPTER 6

Results and discussion

6.1 Experimental results

With the final experimental setup for simple drops we used two constricted capillaries to collect data on 78 drops for the first capillary and over 200 for the second. Both capillaries have the radius in the straight part $r_s = 0.58$ mm. In the constricted part, the radii are slightly different because the process in which the constrictions are made are not able to exactly reproduce the same result. The first capillary has a constriction radius of $r_c = 0.29$ mm and and the second has $r_c = 0.26$ mm. For the first capillary Ca ranged from $8 \cdot 10^{-4}$ to $1 \cdot 10^{-2}$ with Re from $2 \cdot 10^{-4}$ to $3 \cdot 10^{-3}$. For the second capillary Ca was from $3 \cdot 10^{-4}$ to $2 \cdot 10^{-3}$ with Re from $8 \cdot 10^{-5}$ to $8 \cdot 10^{-3}$. We looked at drops with the same size as the capillary to bigger drops that when deformed inside capillary had length about two and half times the capillary diameter. The range of drop speeds resulted in a wide range of transit times from 8 seconds to 11 minutes. Snapshots of two similarly sized drops passing through the two different capillaries are shown in Figure 6.1.

For all the experiments, we extracted the position of the center of mass, front and back end for each frame, as well as the surface area and volume. The data extraction was done using a Matlab script written by Dr. Alexandre Vilquin. For the first capillary images were taken at 50 frames per second, and for the second capillary one frame was taken every second. The velocity in each frame was calculated by fitting a polynomial to the adjacent points and using the gradient. For the first case, a first degree polynomial for 20 prior and subsequent points was used, and for the second case we used a third degree polynomial for ten prior and subsequent points. The polynomial used was different for the two cases because of the difference in frame rates. For the two examples shown in Figure 6.1 the extracted position and speed expressed with Ca for the back part, center of mass and front part of the drop as well as the surface area and volume, is shown in Figure 6.2 for the first capillary and Figure 6.3 for the second. For all the experiments, independent of Ca, the maximum velocities for the front and back part, were approximately one and a half to twice as big as the maximum velocity of the center of mass. As the drop enters the constriction the surface area is increased and when the drop exits the surface area returns to approximately the same value, shown in Figures 6.2c and 6.3c, which is what we would expect since some kinetic energy should be converted to and from interfacial energy as the drop is squeezed through the constriction [80].

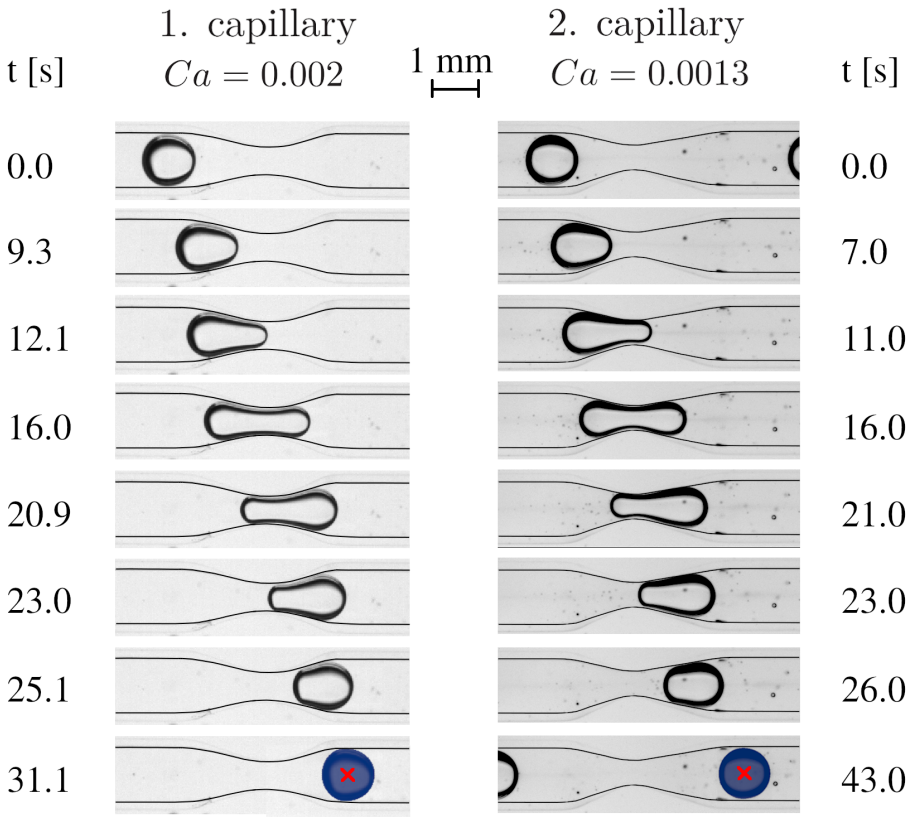

Figure 6.1: Snapshots from the experiments on simple drops. On the left we see an example of an experiment with $Ca = 0.002$ and drop volume $V = 3.8$ mm^3 in the first capillary and on the right the snapshots are from the second capillary with $Ca = 0.0013$ and drop volume $V = 3.6$ mm^3. In the bottom row, the drop found with the drop tracking script is overlayed and the center of mass is marked. The time t in seconds is given on the side of each image, and in the top center a length scale is given.

We expect the drops to have constant volume throughout the capillary, but Figures 6.2d and 6.3d show that this is not the case. The data suggests that the drop loses mass as it enters the constriction and gains mass as it exits. This is not likely to be correct and there are a few contributing factors that can explain these measurements. The fluctuations in the surface area, which are smaller than the difference between the smallest and biggest volume, are smallest when the drop is inside the constriction and mostly comes from inaccuracies when tracking the drops. These inaccuracies come from errors in the numerical integration when volume and area is calculated and in some cases particles that are in the glycerol are thought to be part of the drop, which can change the drop profile. In the images of the second capillary shown in Figure 6.1 these particles can be seen. The capillaries were not perfectly axisymmetric and the volumes were calculated assuming that they were, but since the deviation from axisymmetry for the capillaries was small we do not consider this to be the main

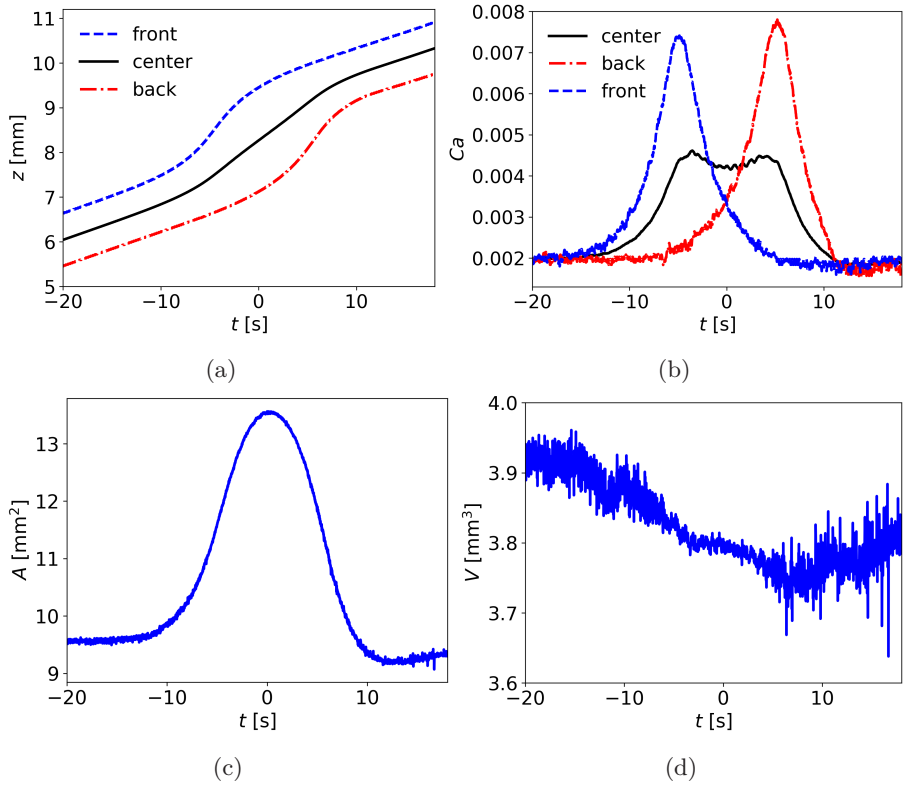

Figure 6.2: Position z, capillary number Ca, surface area A and volume V as function of time for one droplet in the first capillary. For the position and capillary number we plot the values for the front end, center of mass and back end of the drop.

cause. The biggest contribution to the error in volume measurement probably comes from the difficulties we faced getting the capillary in focus. Because of the fragility of the glass capillaries few adjustments could be made to the alignment of the capillary with breaking the glass. We could ensure that the constriction was in focus by adjusting the camera focus, but one end of the capillary was always closer to the camera than the other.

The transit time, which we defined as the time it takes for the drop to move from a position which is $2.5 \cdot r_s$ in front of the contriction entrance to $2.5 \cdot r_s$ after the constriction exit was extracted for all the drops. The transit time in seconds τ_s and drop speed in the straight part of the capillary is shown in Figure 6.4. As expected increasing the speed of the drop reduces transit time. Since increasing the drop speed would also decrease the transit time in a straight capillary, we can make the transit time dimensionless by scaling with the capillary radius r_s and drop speed U to better see how changing the ratio of viscous and surface tension forces changes transit time. The non-dimensional transit time τ as function of Ca is shown in Figure 6.5 for experiments and simulations, but the simulations will be discussed later. We can see that as

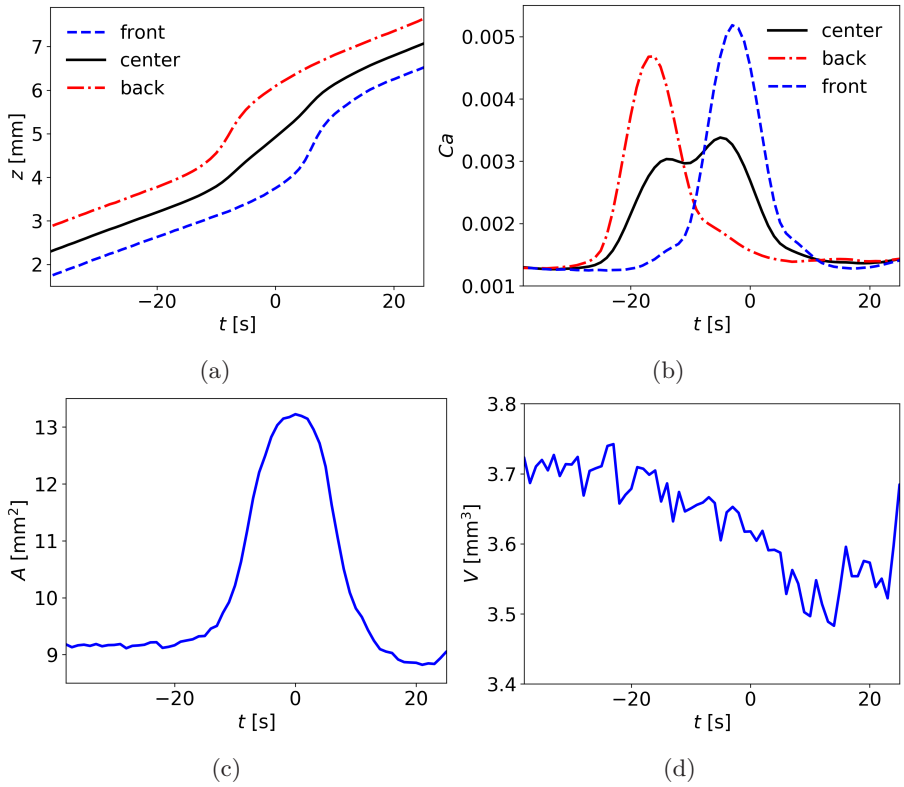

Figure 6.3: Position z, capillary number Ca, surface area A and volume V as function of time for one droplet in the second capillary. For the position and capillary number we plot the values for the front end, center of mass and back end of the drop.

Ca is reduced the non-dimensional transit time is also lowered, but this effect is small compared to the spread of the data. These transit times also include different drop sizes and the size does not seem to have any effect on τ. We only looked at drops of different sizes on the low end of the Re and Ca range, which could partly explain why. At such low Re, the curvature of the front and back part of the drop does not depend on drop size, so the Young–Laplace pressure induced by difference in curvature of the front and back parts [81], would not depend on size. One would expect that as Ca is reduced, the surface tension of the drop would eventually prevent the drop from deforming enough to be able to fit through the constrictions, but from these experimental data this does not appear to be the case. We tried reducing the driving pressure by lowering the reservoirs for the input fluids, but instead of seeing any signs of clogging the drops would start traveling backwards. So in order to see clogging of the capillaries, we would need to able to apply a smaller driving pressure than we were able to do. Another idea would be to use a combination of liquids with a higher surface tension to viscosity ratio so that the driving pressure could be higher.

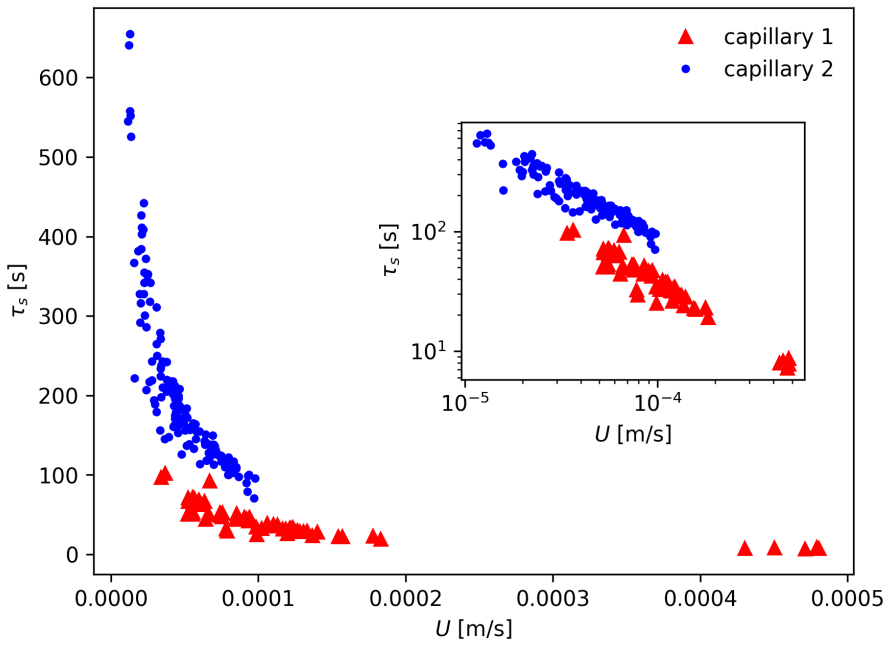

Figure 6.4: The experimental transit time τ_s in seconds as function of drop speed U far away from the constriction for capillary 1 and 2. The inset shows the same data using logarithmic axes.

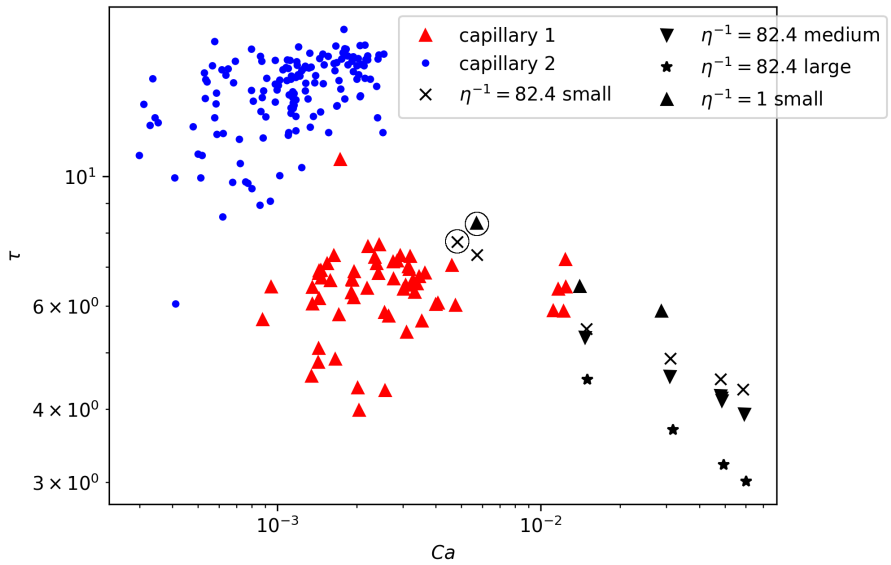

Figure 6.5: The dimensionless transit time τ as function of Ca for experiments and simulations. Capillary 1 and capillary 2 is the data from the two experimental setups and the other markers show the numerical results. Since the transit time of clogging cases is infinite, the clogging cases have been added to the plots and marked with a circle.

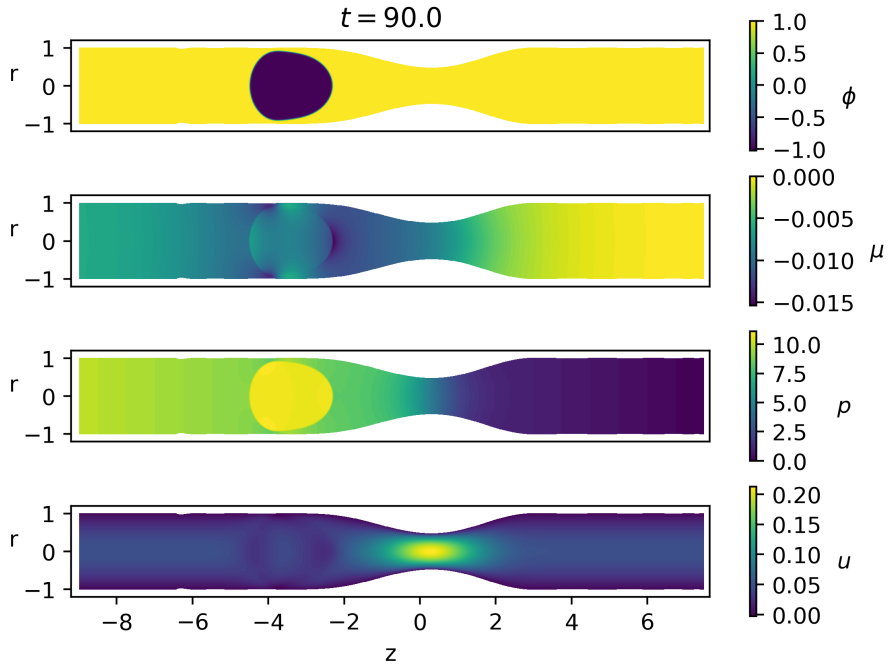

Figure 6.6: Concentration ϕ, chemical potential μ, pressure p and the magnitude of the velocity $u = \sqrt{u_r^2 + u_z^2}$ for a simple drop with $Cn = 0.01$.

6.2 Numerical results

In all simulations, we have a no-slip boundary condition on the wall, and set the inlet and outlet pressures p_i and p_o. For the chemical potential we use the no fluxes of chemical potential condition (2.16). For the concentration we set the contact angle $\theta_c = 90°$ at the inlets and outlets and $\theta_c = 180°$ on the walls. The drops are initialized at least five times the tube radius to the left of the constriction so that they are given enough time to reach a stable shape before entering the constriction. The concentration, chemical potential, pressure and velocity field can be extracted and are as shown in Figure 6.6.

To control the capillary number in the simulations the straight forward approach would be to set the pressure difference $\Delta p = p_i - p_o$ such that the velocity of the drop is 1, and then simply the set the parameter Ca equal to the capillary number we want to simulate. However since parasitic velocities become an increasing problem when the Ca parameter is low, we instead set the parameter to $Ca \sim 1$, and adjust Δp to reduce the velocity of the drop. The effective capillary number in the simulations is then found by multiplying the input parameter for Ca with the drop velocity.

Before presenting the numerical results, we first confirm that the interface thickness we choose does not change the results for sufficiently small Cn. To confirm this we ran two simulations, one with $Cn = 0.01$ and the other with $Cn = 0.02$. The position z as function of time t of the back, center of mass and front parts of the drop is shown in Figure 6.7. It is clear that changing Cn between these two values do not change the results. For all

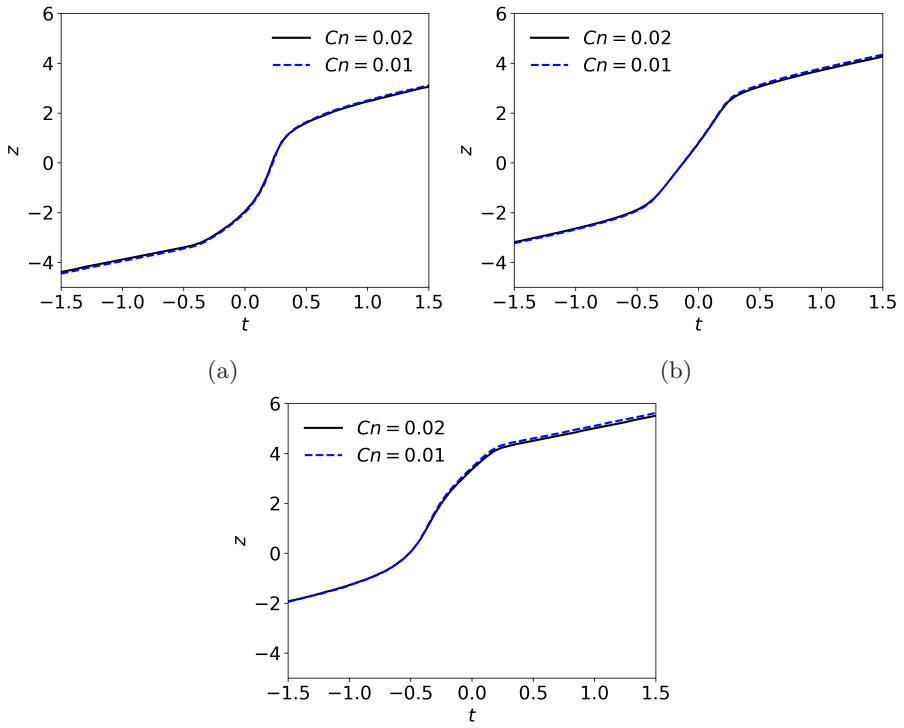

Figure 6.7: Position as a function of time for simulations with $Cn = 0.02$ and $Cn = 0.01$ for the a) back, b) center of mass and c) front of the drop.

the simulations discussed in this chapter we therefore keep the same interface thickness, $Cn = 0.01$.

6.3 Comparing experiments and simulations for a simple drop

Difference in Ca

When first comparing simulations with experiments, the viscosity ratio and effective capillary number was set to be the same in the simulations as in the experiments. Looking at the drop shape in the straight part of the capillary, we found the drops were more elongated in the simulations than in the experiments, which meant that the capillary number in the simulations were higher than in the experiments. By running a series of numerical experiments for drops at various volumes and capillary numbers we found that the in order to get the same drop shape in the simulations as in the experiments we have to multiply the capillary number by a non constant factor. To get the same drop deformation in the simulations as in experiments with Ca from $\sim 10^{-3}$ to $\sim 10^{-2}$, the capillary number in the simulations needed to be multiplied with a factor from 2.9 to 4.6 for experimental Ca from $\sim 10^{-3}$ to $\sim 10^{-2}$. Using this method for

$Ca < 10^{-3}$ does not work, because when Ca is sufficiently small the drops take on a symmetrical shape and the deformation no longer depends on Ca.

So in order to compare simulations with experiments, we compare experiments with simulations that have the same drop shape in the straight part of the tube under the assumption that this ensures the ratio of viscous and surface tension forces are the same in the simulation and experiment. This also means we are only able to compare results for $Ca > 10^{-3}$.

Deformation and transitory characteristics

To look at how experiments and simulations compare in terms of deformation in different parts of the constriction, we consider an experiment were $Ca = 0.011$. Since the viscosity of the continuous fluid should be 82.4 times greater than the viscosity of the drop, we set $\eta^{-1} = 82.4$ in the simulations as well. In Figure 6.8 images of the drop from simulations and experiments are shown in the same place of the constriction, and the nondimensional time is shown next to each image. $t = 0$ is defined to be when the center of mass of the drop is in the middle of the constriction. We can see that the drop shape is similar at all stages of the constriction except for the second to last image. Here the experimental drop has a flat back end, whereas in the simulation it does not. In the simulation, the third and sixth rows resemble mirror images of each other, which is in agreement with some previous work by Zhang and colleagues [81, 82]. For the experiment, rows three and six are not mirror images but the drop has a flat rear end as it exits the constriction, which has also been found by others [41] as well as for both air bubbles [15] and capsules [15, 46, 62]. Looking at the time between each image, it is also clear the that experimental drop spends nearly twice as long time inside the constriction.

Because of the big difference in transit time between the simulations and experiments, we tried changing η in the simulations to see how that changed the results. By setting the two viscosities to be equal, $\eta^{-1} = 1$, we observed that both drop deformation and time spent inside the constriction was in closer agreement with the experiments. In Figure 6.9 we show the deformation for a simulation with $\eta^{-1} = 1$ and the same experiment that was shown in Figure 6.8. In all the stages the drop shape is similar. Especially for the second to last image it is clear that the drop shape for $\eta^{-1} = 1$ is much closer to the experiments, than is the simulation with $\eta^{-1} = 82.4$. The transit times are still not the same, but the experimental drop now only spends about 12% more time inside the constriction than the simulated drop.

We then look at how the three cases compare in time. To plot the experiment and simulations in the same plot, we also scale the length with r_s. The position is set to $z = 0$ in the middle of the constriction. The resulting Ca as function of time is in Figure 6.10 and position as function of time is in Figure 6.11. For all cases we see that the rear end has a higher maximum velocity than the front end. This is in agreement with what has been found for air bubbles and capsules under constant flow rate [15]. It is also clear that the simulation with $\eta^{-1} = 1$ is much more similar to the experiments than the simulation with $\eta^{-1} = 82.4$. When inside the constrictions, the drop in the simulation with $\eta^{-1} = 82.4$ moves more than twice as fast as the experiments, whereas for the simulation with $\eta^{-1} = 1$ the drop has approximately the same maximum velocity.

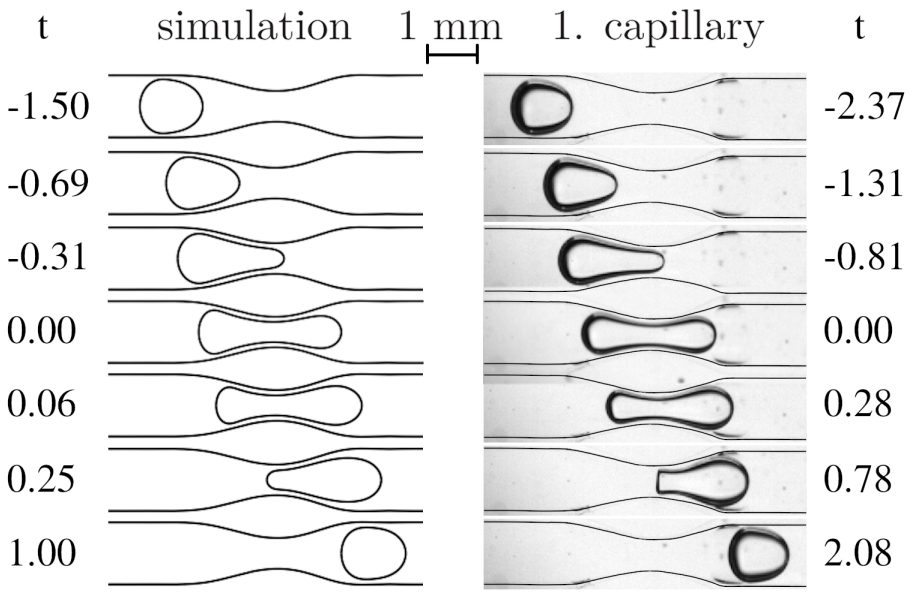

Figure 6.8: Drop shape in different parts of the constriction for simulation with $\eta^{-1} = 82.4$ on the left and experiment on the right for experimental capillary number $Ca = 0.011$. The time is shown on the sides.

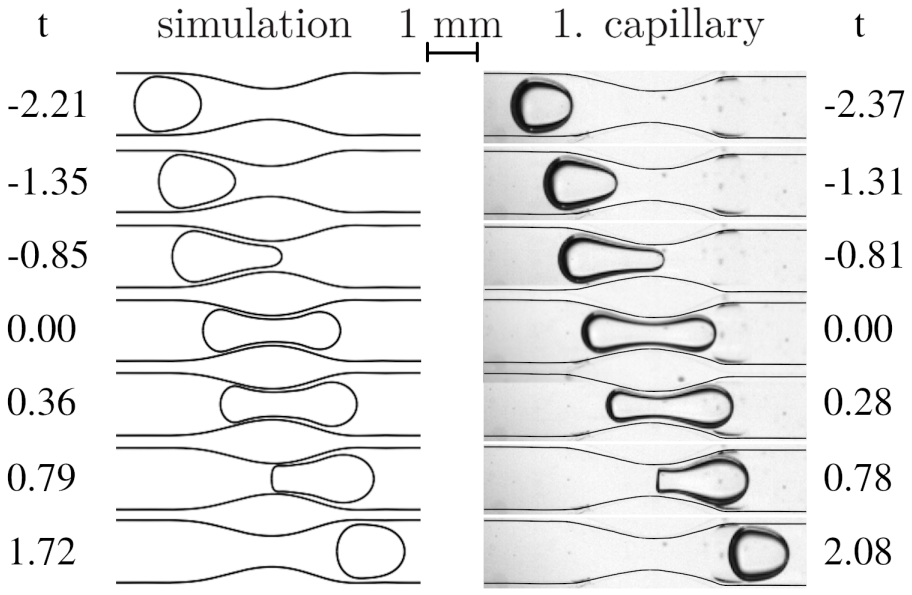

Figure 6.9: Drop shape in different parts of the constriction for simulation with $\eta^{-1} = 1$ on the left and experiment on the right for experimental capillary number $Ca = 0.011$. The time is shown on the sides.

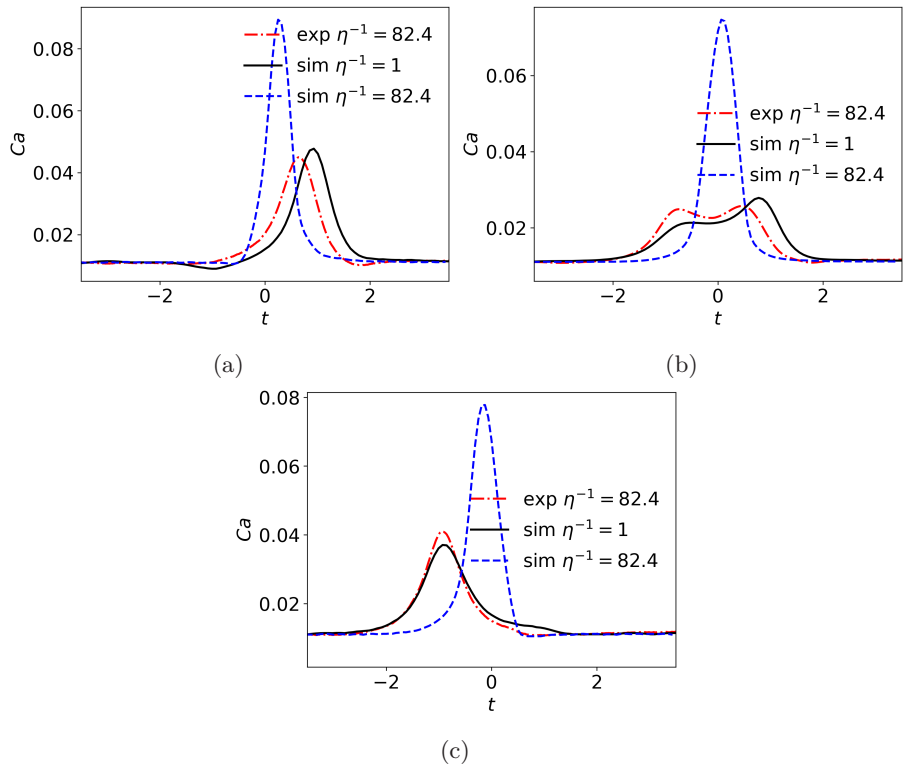

Figure 6.10: Drop speed expressed with Ca as a function of time for experiment and simulations with $\eta^{-1} = 1$ and $\eta^{-1} = 82.4$ for the a) back part, b) center of mass and c) front part measured at $r = 0$.

Since we did not measure the velocity field in the experiments, we cannot calculate the viscous dissipation rate. However from the simulations we have the necessary data to calculate the viscous dissipation rate $\dot{R}_\eta$ and the rate of diffusive fluxes of the chemical potential $\dot{R}_\mu$. The dissipation rates for $\eta^{-1} = 82.4$ is shown in Figure 6.12. We see that $\dot{R}_\eta$ is always much greater than $\dot{R}_\mu$. Some energy is also converted to interfacial energy as the drop enters the constriction and when the drop exits the interfacial energy is reduced. In Figure 6.13 we show how the rate viscous dissipation and surface area for the two different viscosity ratios change over time, in this figure we have scaled the surface area and $\dot{R}_\eta$ with the values far away from the constriction. For $\eta^{-1} = 1$ the viscous dissipation is almost antisymmetric around $t = 0$, but for $\eta^{-1} = 82.4$ this is not the case at all, instead the initial reduction is about eight times smaller than the increase we observe as the drop exits the constriction. It is not surprising that the difference is so big considering that the maximum velocities in the $\eta^{-1} = 82.4$ is about twice as big as those for $\eta^{-1} = 1$ in addition to the viscosity difference.

When the drop is not close to the constriction the rate of viscous dissipation is constant and the majority of the viscous dissipation occurs close the wall in the middle of the constriction as shown in Figure 6.14a. This is what we expect

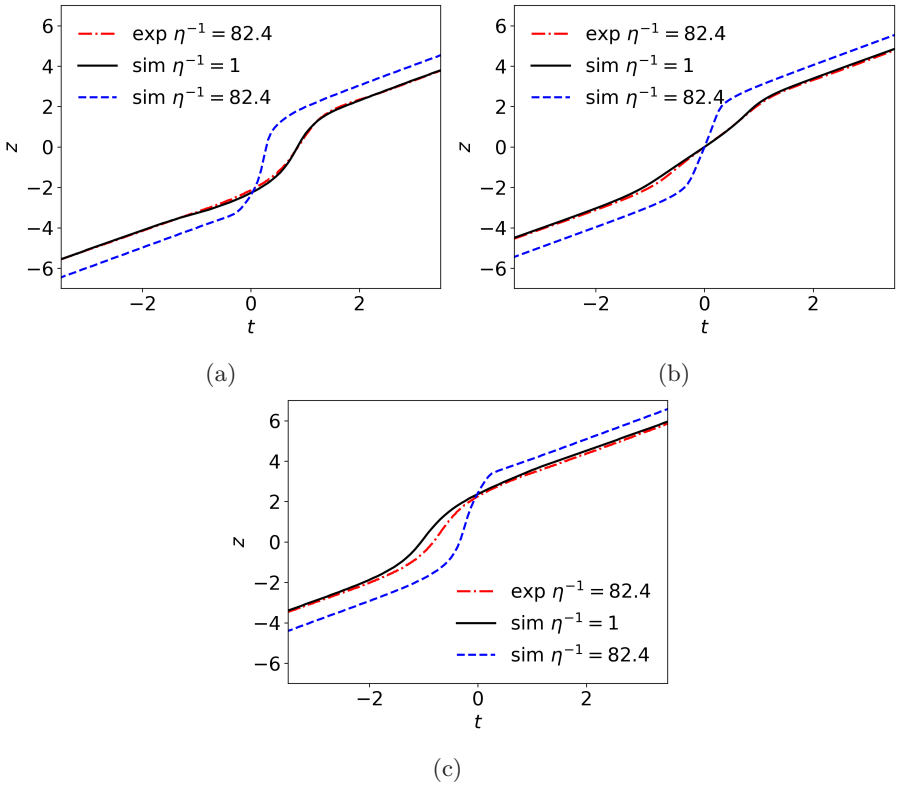

Figure 6.11: Position as a function of time for experiment and simulations with $\eta^{-1} = 1$ and $\eta^{-1} = 82.4$ for the a) back part, b) center of mass and c) front part measured at $r = 0$.

since the velocity gradients are biggest in the constriction. The minimum occurs when the tip of the drop which is less viscous that the surrounding fluid is in the middle of the constriction, shown in Figure 6.14b. As the drop is in the middle of the constriction the $\dot{R}_\eta$ is distributed as shown in Figure 6.15a with the majority of the dissipation happening inside the droplet in the middle of the constriction. The maximum is when the rear end of the drop is in the middle of the constriction and the more viscous surrounding fluid is being pushed in to replace the less viscous drop, shown in Figure 6.15b.

Why do the simulations and experiments not agree?

It is clear that for $\eta^{-1} = 82.4$ the numerical simulations and the experiments produce very different results. Even in the straight part of the capillary the drop deformation was different, but for $\eta^{-1} = 1$ the results are much more similar. It is tempting to argue that there is an error in how the code handles viscosity ratios different from 1, and that the results for $\eta = 1$ is similar to the experimental results because the viscosity ratio does not play that much of a role. However we confirmed that the code works on viscosity ratios $\eta \neq 1$ with the drop relaxation test with $\eta = 10$ and the drop spreading test using

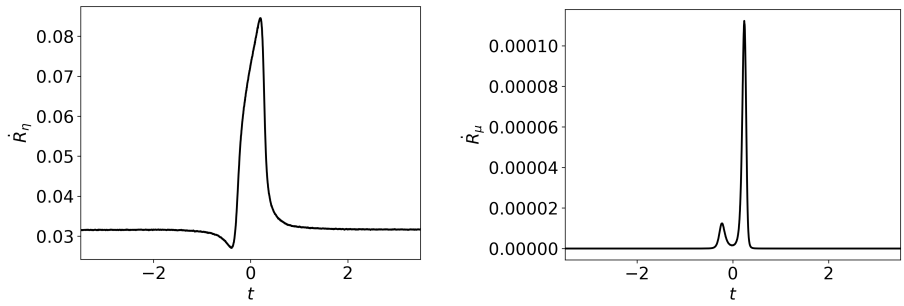

(a) (b)

Figure 6.12: Viscous dissipation rate $\dot{R}_\eta$ (a) and diffusive fluxes of chemical potential $\dot{R}_\mu$ (b) for simulation of a simple drop with $\eta^{-1} = 82.4$ and $Ca = 0.05$.

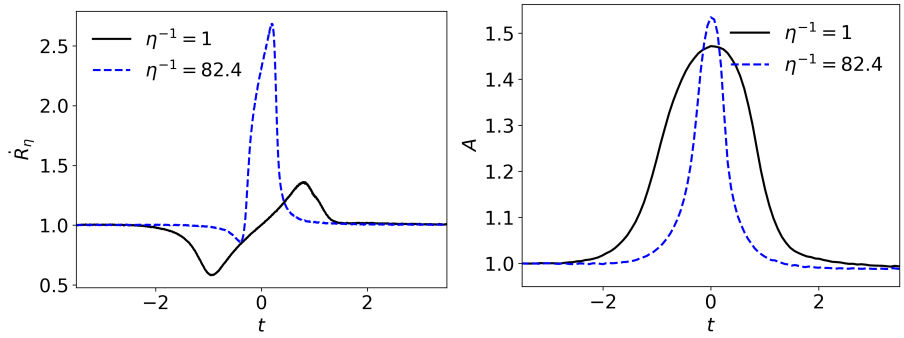

(a) (b)

Figure 6.13: Viscous dissipation $\dot{R}_\eta$ (a) and surface area A (b) for simple drops with $\eta^{-1} = 1$ and $\eta^{-1} = 82.4$ and $Ca = 0.05$. $\dot{R}_\eta$ and A are scaled with their values far away from the constriction.

$\eta = 50$. We also compared the drop shape in a straight channel for $\eta = 10$ with published results from simulations with the Boundary Integral method [42] and got good agreement, so the code is definitely able to handle the different viscosities.

One possibility is that the film between the drop and the wall is not adequately resolved. In the straight part of the capillary, we expect the film thickness to follow $\sim Ca^{2/3}$ [5]. However we have kept $Cn = 0.01$ in all simulations, so when the film thickness relative to the interface thickness becomes small problems can arise because the film is not resolved sufficiently.

If the difference can not be explained by an error in the code, it either stems from the experiments or both. One possibility is that either the viscosity or surface tension of the sunflower oil + PGPR solution was not measured correctly. However the surface tension measured was in close agreement with [56]. The measured viscosity is about 25% greater than the viscosity of sunflower oil without PGPR at 20° C [23], which seems reasonable since the surfactant

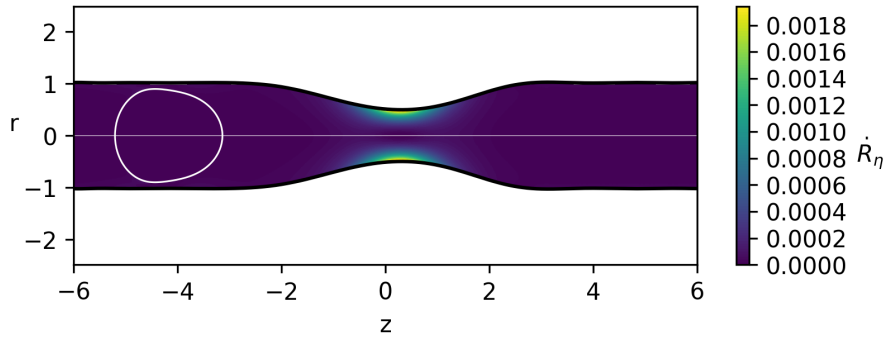

(a)

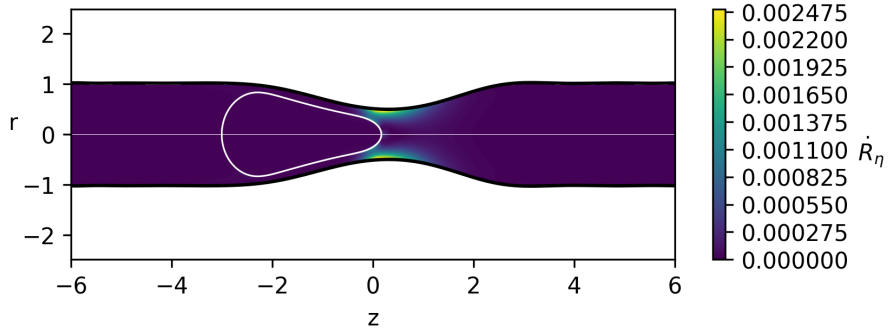

(b)

Figure 6.14: Rate of viscous dissipation $\dot{R}_\eta$ for simple drop with $\eta = 82.4$ and $Ca = 0.05$. The interface of the drop is shown by the white outline and has the same thickness as the drop interface, which here is given by $Cn = 0.01$. In (a) the drop is in the straight part and in (b) the front end of the drop is in the middle of the constriction and it is here the minimum rate of viscous dissipation is found.

is expected to increase the viscosity. It was also obvious when handling the sunflower oil solution that it was much more viscous than water, and if there is an error in the measured viscosity it can be nowhere near big enough to explain why we needed to change the viscosity ratio by a factor of 82.4 in the simulations.

Since the viscosity and surface tension was measured under different conditions than the experiments, it is possible that conditions the droplet undergoes in the experiments has an effect on the true values. For example if there are gradients in the surface tension marangoni effects that can affect the drop deformation and the curvature induced pressure drops at the front and back part of the drops [58] could play a role. The use of surfactants can also have significant effect on the boundary conditions on the drop [31] and if it is altered to a no-slip condition, the dispersed phase would behave as if it was more viscous. Which if the case, would explain why the drops behave as if their viscosity is much closer

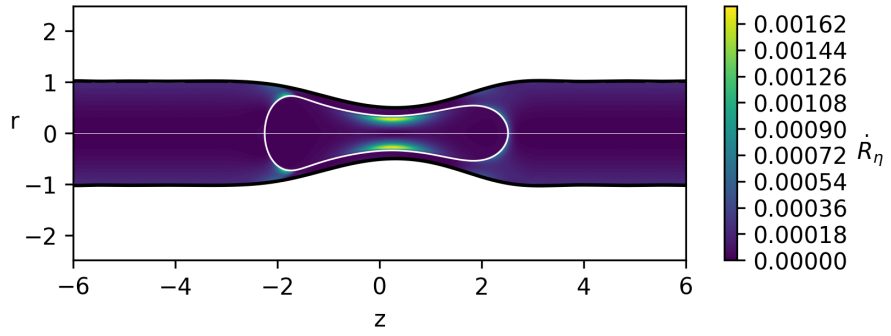

(a)

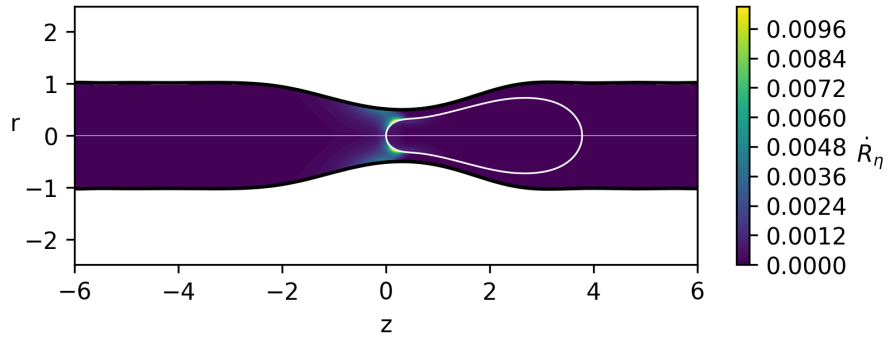

(b)

Figure 6.15: Rate of viscous dissipation $\dot{R}_\eta$ for simple drop with $\eta = 82.4$ and $Ca = 0.05$. The interface of the drop is shown by the white outline and has the same thickness as the drop interface, which here is given by $Cn = 0.01$. In (a) the drop is in the middle of the constriction (b) the back end of the drop is in the middle of the constriction and it is here the maximum rate viscous dissipation is found.

to the continuous phase than what we measured. Another possible explanation could be shear thinning of the sunflower oil in the film between the drop and the capillary wall, but since the viscosity measurement was taken with shear rates from 1 s^{-1} to 100 s^{-1} the film thickness would have to be orders of magnitude smaller than the film thicknesses we observed, which were 10 μm or larger.

Optical distortions are also worth considering because even though it would not affect the transit time it could possibly contribute to errors in the measured drop deformation and film thickness. Glycerol has a refractive index of $n_{gly} = 1.47$ [30], glass typically has $n_{gla} = 1.49$ and sunflower oil $n_o = 1.47$ [1]. Since the refractive indices are so similar, the optical distortion [14] that arises when light moves from one medium to another is not big enough to explain why the drop deformation we see in the straight part of the capillary is not what we expect. The error in the film thickness measurements caused by optical distortion is also not big enough for the actual film thickness to be several times

smaller than what measured, which is what would have to be the case for shear thinning to happen.

One test we could have done to control whether the surface tension and viscosities are as expected, would be to have a drop in shear flow and compare the deformation we observe with analytical results [27], however we did not think of this until after the experiments were done.

6.4 Capillary clogging

To investigate capillary clogging numerically, we ran a series of simulations for $\eta^{-1} = 82.4$ and $\eta^{-1} = 1$ by reducing the effective capillary numbers until we observed that the drop got stuck in the constriction and as a result the flow velocities were greatly reduced. For $\eta^{-1} = 82.4$ and $Ca = 4.3 \cdot 10^{-3}$ we observed that the droplet got stuck in the constriction. For $Ca = 5.8 \cdot 10^{-3}$ there was no clogging, but the transitory characteristics were different from drops with higher capillary numbers because it was almost clogging. In Figure 6.16, we show how the position of the front, center of mass and back parts of these two cases as well as one with $Ca = 3.1 \cdot 10^{-2}$ change over time. In Figure 6.17, we see the speed expressed with Ca as function of time. The almost clogging case takes longer time to get the front part of the drop past the narrowest part of the constriction, but once it has passed this point the two cases behave similarly. For $\eta^{-1} = 1$ the clogging was found at $Ca = 5.8 \cdot 10^{-3}$, which is slightly higher than for the other case but supports the claim that the viscosity ratio does not play an important role in determining the capillary number at which clogging occurs [86]. How the speed and position of the different parts of the drop behaves, is similar to the $\eta^{-1} = 82.4$ drops for the clogging and almost clogging cases. As predicted by the Young–Laplace relation sufficiently high surface tensions result in the drop getting stuck. More generally we find that for sufficiently low capillary numbers, Ca controls transit time which is in qualitative agreement with Zinchenko and Davis [86]. However since they looked at very different viscosity ratios and geometry than us, we do not expect our results to follow the same power-law that they found. These results do not reflect what we found experimentally, where we did not observe any effect of Ca on how the drops are squeezed through.

The transit time of non clogging, almost clogging and clogging cases for $\eta^{-1} = 82.4$ and $\eta^{-1} = 1$ were extracted and are plotted in alongside the experimental data in Figure 6.5. These results are different than the experimental data, since when Ca is reduced and we get closer to clogging, the transit time increases. The observation of almost clogging drops, suggests that we were far away from observing clogging experimentally, because we did not see any drop that exhibited this behavior. When the capillary number is increased, less time is spent inside the constriction and for sufficiently big Ca one would expect the non-dimensional transit time to be independent of Ca because the interface is so easily deformed. It is therefore possible that this is the explanation for why the transit time in the experiments where independent of Ca, and if we were to run simulations for higher capillary numbers than those we have presented we would be able to confirm if this is indeed the case.

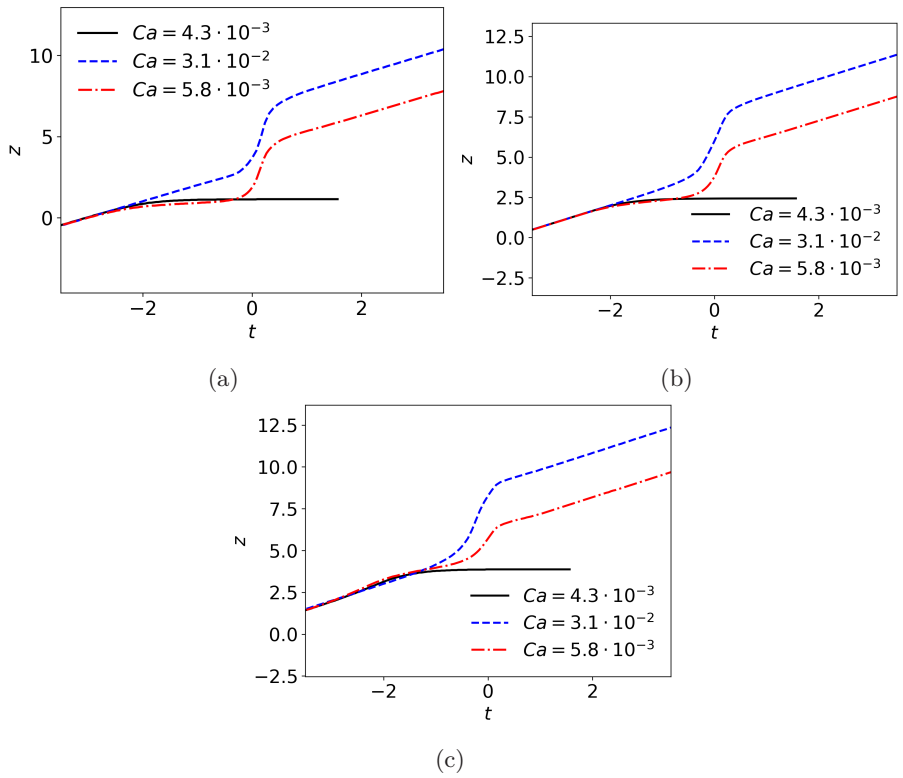

Figure 6.16: Position as a function of time for simulations for a clogging, almost-clogging and non-clogging drop for the a) back part, b) center of mass and c) front part measured at $r = 0$.

6.5 Compound drops

Compound drops were created by placing a smaller drop inside the simple drop. In this project we restrict ourselves to one combination of the drop radii r_1 and r_2. We also only consider cases where the viscosity is equal in all three phases, so any comparison to simple drops are done for $\eta^{-1} = 1$. To most clearly see how a compound drop is different from a simple drop, we first look at a compound drop where the capillary number of the internal and the outer drop are the same as for the simple drop. Since we no longer are comparing the numerical results with the experiments, we change to a symmetric mesh, were the constriction wall can be described with a $\cos(z)$ function. For this constriction, the length and is the same as previously. To see how adding an extra drop inside the simple drop changes the dynamics we compare the deformation in the different parts of the constriction in Figure 6.19 for a compound drop where the capillary number for the outer and inner interfaces Ca_1 and Ca_2 are the same. There is almost no difference in the deformation or transit time. This means that the energy required to deform the inner drop is much smaller than the bigger drop which is not surprising since the required deformation is much smaller. In the straight part of the capillary, the inner drop always stays toward the front

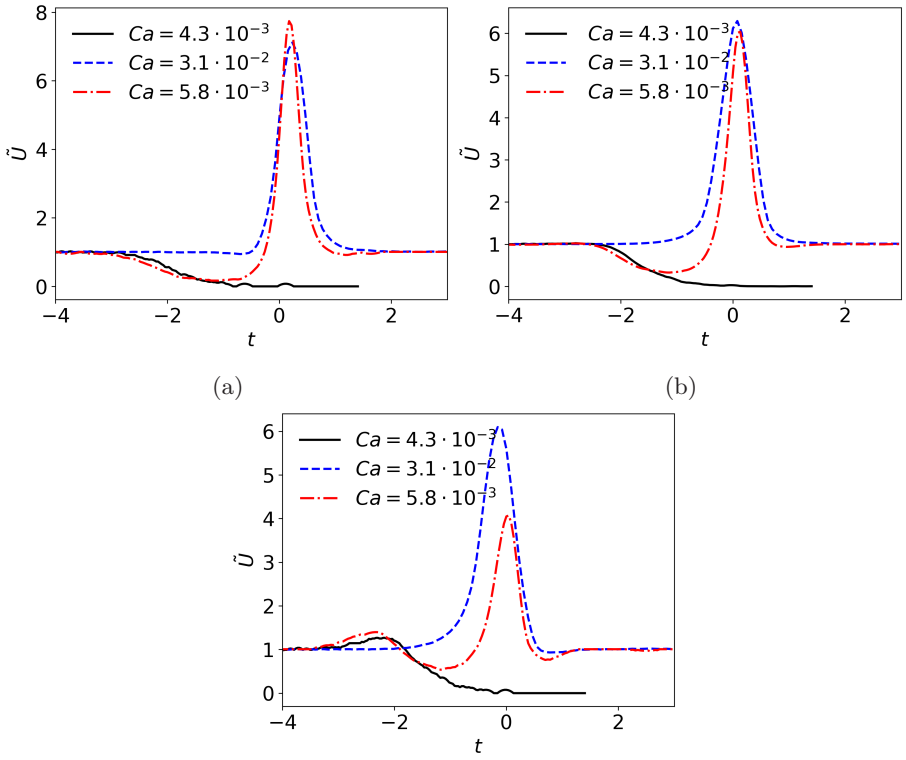

Figure 6.17: Ca as a function of time for simulations for a clogging, almost-clogging and non-clogging drop for the a) back part, b) center of mass and c) front part measured at $r = 0$.

part of the outer drop, which is in agreement with what we observed for the few compound drops we were able generate experimentally, see Figure 5.10. In Figure 6.20 we also see that the speed of the outer interface as a function of time is almost the same as for the simple drop for the back, center of mass and front part of the drop. So simply adding a drop which has the same capillary number as the outer drop only slightly changes the results when the viscosity is the same.

Further we can explore how changing the ratio of the capillary numbers $\tilde{Ca} = Ca_1/Ca_2$ changes the drop deformation. In Figure 6.21 we compare the drop deformation of two drops that have the same capillary number for the inner drop Ca_1, but different the outer capillary numbers Ca_2 so that $\tilde{Ca} = 10$ and $\tilde{Ca} = 2$ for the two cases. We see that the difference in the deformation of the outer drop is very big. Looking at the fourth image it is clear that these cases are very different, for $\tilde{Ca} = 10$ it almost looks like the part in front of the inner drop is about the break free. As for the simple drops, the outer capillary number also affects the transit time. Similarly we can also look at how changing the inner capillary number affects the results while keeping the outer capillary number constant. In Figure 6.22 drops with $\tilde{Ca} = 2$ and $\tilde{Ca} = 1$ are shown

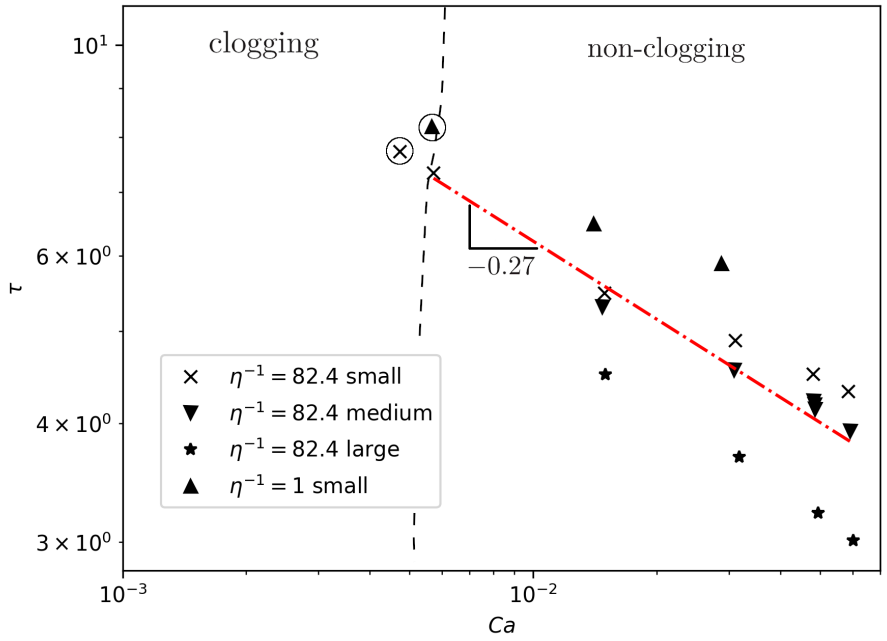

Figure 6.18: The dimensionless transit time τ as function of Ca for the simulations. Since the transit time of clogging cases is infinite, the clogging cases have been added to the plots and marked with a circle. The dashed line shows where the transition from non-clogging to clogging happens.

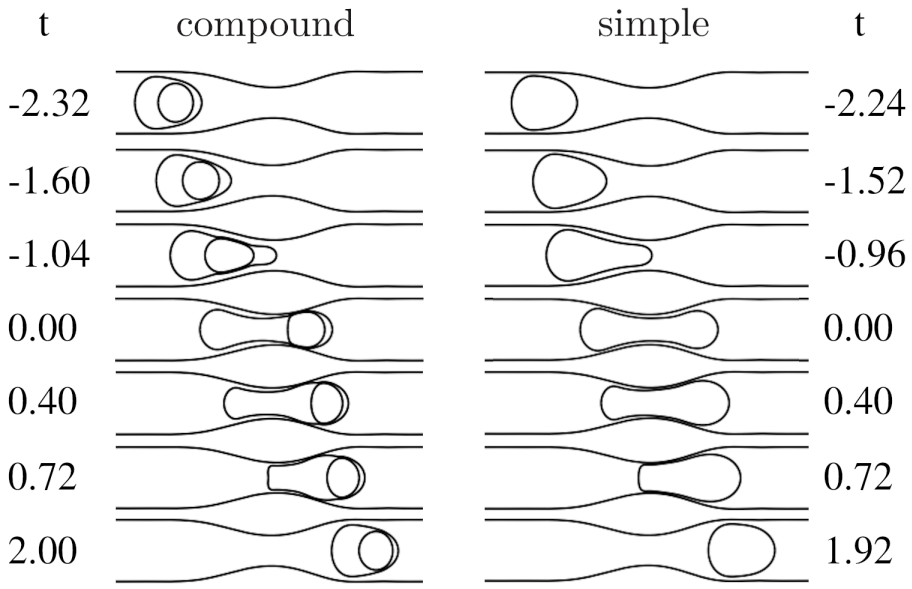

Figure 6.19: Drop shape in different parts of the constriction for simulation with compound drop on the left and simple drop on the right. The time is shown on the sides.

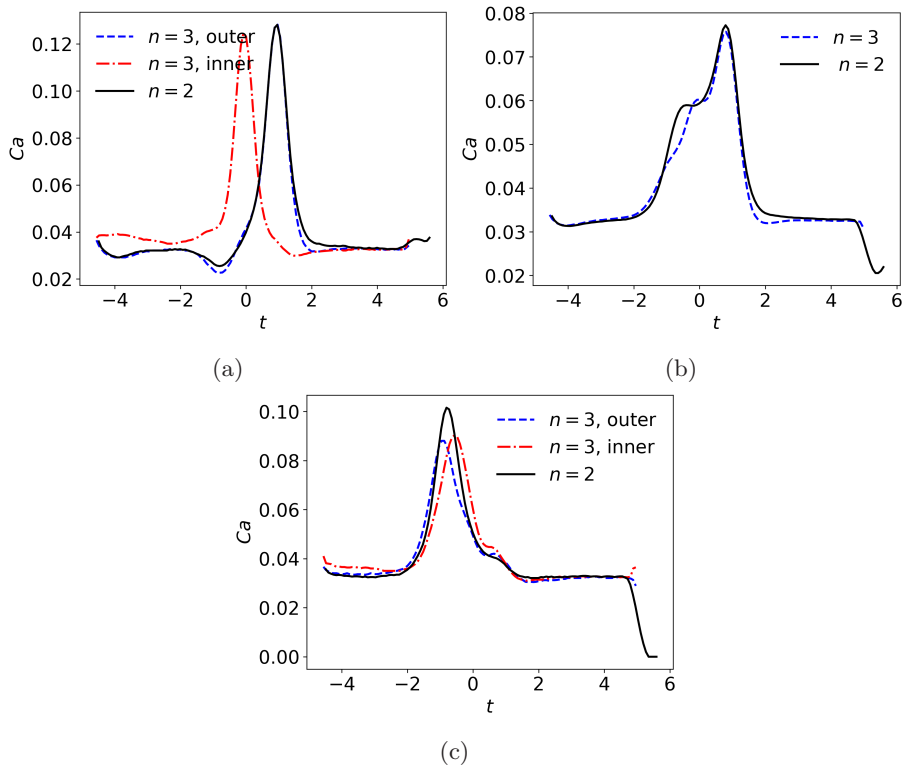

Figure 6.20: Drop speed given by Ca for simple $n = 2$ and compound $n = 3$ drop with equal viscosity in all phases as a function of time for the a) back part, b) center of mass and c) front part measured at $r = 0$. The interface of the inner drop is called inner and the interface of the outer drop is called outer.

next to each other and there is almost no difference in the drop shapes when we look at the different parts of the constriction. The transit times are also similar, but higher capillary numbers for the inner drop does lead to a reduction in transit time. Since the inner drop does not have to deform much compared to the outer drop, it is not surprising that changing Ca_2 has a smaller effect on the results than changing Ca_1, and we expect that the role of Ca_2 very much depends on the size of the inner drop relative to the constriction width.

Similarly as we did for the simple drops, we wanted to get an overview of how changing the drop parameters changes the transit time. Since the compound drops have an extra capillary number, which introduces another parameter that can be changed, we kept the sizes of the inner and outer drops constant for all the simulations. The transit time τ as a function of the outer and inner capillary number Ca_1 and Ca_2 is shown in Figure 6.23. There is a tendency for the transit time to increase as the capillary numbers decrease, but this trend is not as clear as is was for the simple drops. The capillary number required for clogging was the same for compound drops with $Ca_1 = Ca_2$ as it was for the simple drop with $\eta^{-1} = 1$. We do not really understand why the relationship between τ and Ca_1 and Ca_2 is not as clear as it was for the simple drops, but

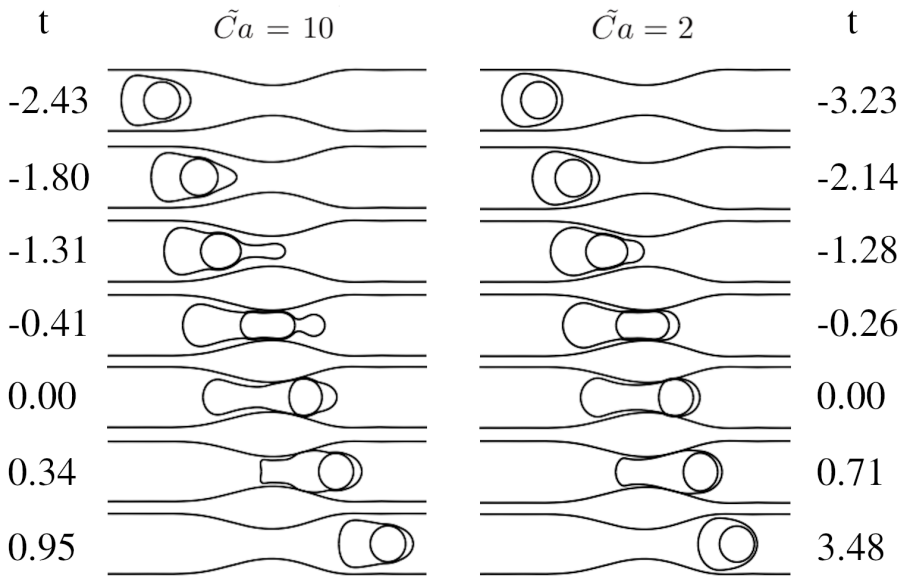

Figure 6.21: Drop shape in different parts of the constriction for simulation with compound drops. On the left $Ca_1 = 0.075$ and $Ca_2 = 0.0075$. On the right $Ca_1 = 0.015$ and $Ca_2 = 0.0075$. The time is shown on the sides.

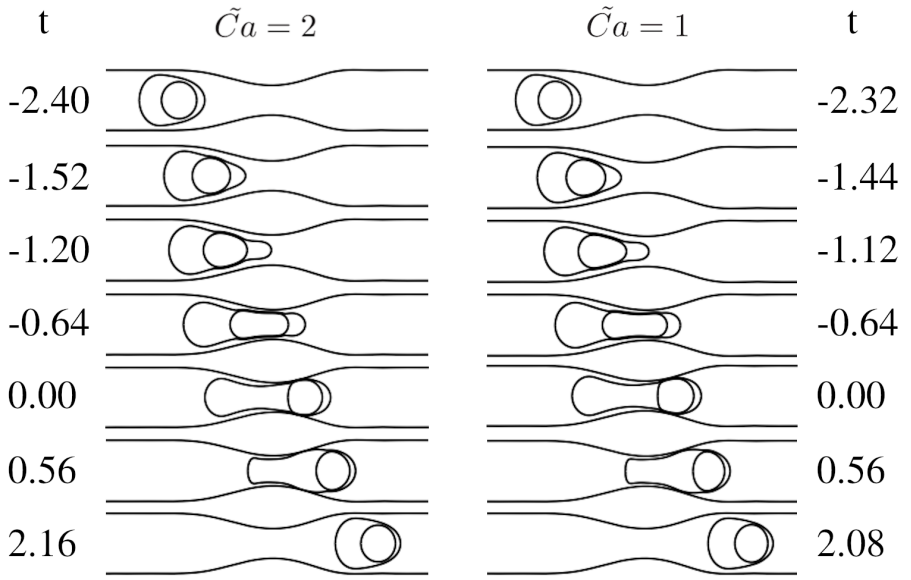

Figure 6.22: Drop shape in different parts of the constriction for simulation with compound drops. On the left $Ca_1 = 0.03$ and $Ca_2 = 0.015$. On the right $Ca_1 = 0.03$ and $Ca_2 = 0.03$. The time is shown on the sides.

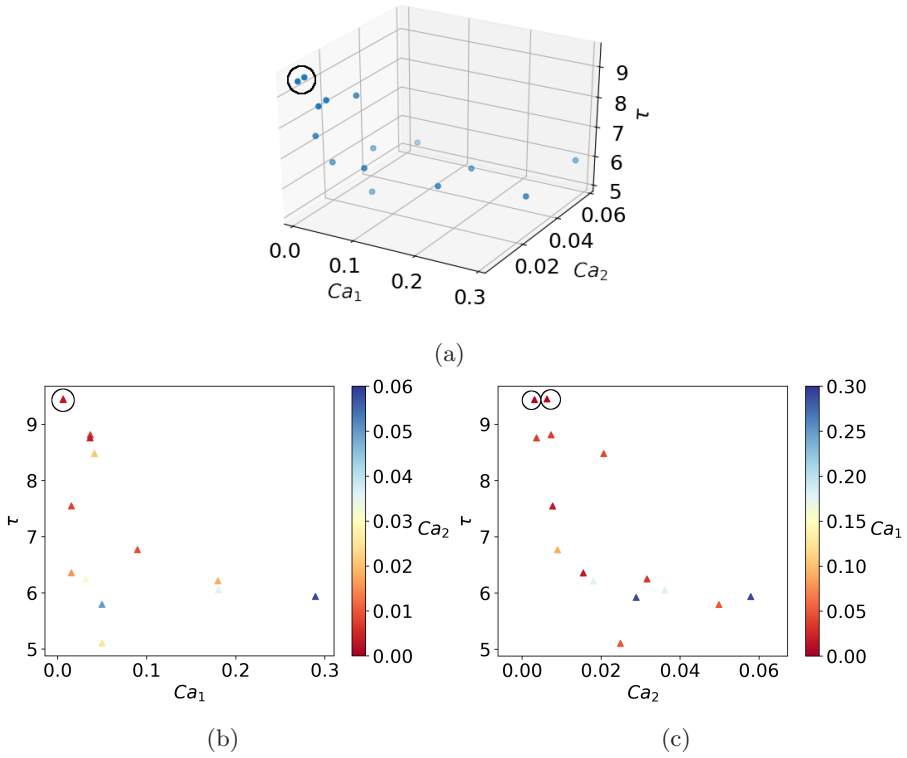

Figure 6.23: The dimensionless transit time τ as function of the capillary numbers for the outer and inner drop Ca_1 and Ca_2. Since the transit time of clogging cases is infinite, the clogging cases have been added to the plots and marked with a circle. In (a) we show the transit time as function of both capillary numbers Ca_1 and Ca_2, in (b) we have collapsed the Ca_2 axis and show τ as a function of Ca_1 where Ca_2 is shown with different colors and in (c) the Ca_1 axis has been collapsed and Ca_2 is shown with colors.

performing more numerical experiments could shed light on why this is the case.

CHAPTER 7

Conclusions

In this thesis, we studied the transit of a drop through a constriction using numerical and experimental methods. About 300 experiments were done on simple drops with Ca from $8 \cdot 10^{-4}$ to $2 \cdot 10^{-3}$ squeezing through constrictions, and the results showed no clear relationship between the capillary number and the non-dimensional transit time. We were not able to produce any examples where the drops clogged the capillary and there was no indication that the drops were anywhere close to the clogging regime. To generate compound drops we tried three different methods, two of which are commonly used is microfluidics, however they are normally used to create smaller drops than what we needed since we were working on the boundaries between micro and millifluidics. The required size of the drops was probably the main cause of our issues with the compound drops.

A Cahn-Hilliard creeping flow model for two-phase flow and one for three-phase flow was implemented using the Finite Element method in FEniCS. The two-phase model was validated using test cases such as Laplace pressure jump for a drop in equilibrium, spreading of a viscous drop on a surface and relaxation of a drop. The only difference in the implementation of these tests are the boundary conditions and initialization of the concentration parameter, which shows one of the advantages of phase field models, their versatility. When simulating simple drops using the same viscosity ratio as in the experiments we found there to be a big difference between the numerical and experimental results, both with respect to drop deformation and transit time. Changing the viscosity ratio to $\eta^{-1} = 1$ in the simulations however changed the results in such a way the numerics and experiments were in much stronger agreement. Looking at the drop shape in the different parts of the constriction they looked almost identical and the transit time was also much more similar. We were not able to determine why the difference is so big for $\eta^{-1} = 82.4$ and so small for $\eta^{-1} = 1$, but the most promising explanation is that the surfactants used in the experiments alter the boundary conditions on the drop. Experiments using different liquids, for example liquids with approximately the same viscosity, or experiments without surfactants could help us understand why the experiments are so different from the simulations.

With simulations we were able to produce clogging, almost clogging and non clogging cases with the simple drop simulations. The clogging occurred at capillary numbers around $Ca = 5 \cdot 10^{-3}$ for both viscosity ratios investigated, which suggests that the viscosity ratio is not an important factor for what capillary numbers lead to clogging and is in agreement with [86]. We were

also able to observe that as the capillary number is reduced towards the values required for clogging, the drop slows down in the first section of the constriction instead of speeding up as it does for $Ca > 4{\cdot}10^{-3}$. Since the experimental results showed no strong relation between non-dimensional transit time and capillary number, it is possible that the experiments showed a different regime than the simulations, a regime where the role of surface tension is so small that reducing the surface tension further has virtually no effect on the non-dimensional transit time.

For compound drops we found that introducing a drop inside of a simple drop does not in itself cause a big change in how the drop is squeezed through the constriction. When we make the capillary numbers for the inner and outer drop different we see a big difference. Especially when the capillary number for the outer drop is several times larger than for the inner drop, because the outer drop is then pushed through the constriction much easier than the inner phase. As we did for the simple drops we did a number of simulations to try to understand how the capillary numbers Ca_1 and Ca_2 affect the transit time of the drops. Similarly to the simple drops the transit time tends to increase as the capillary numbers are reduced.

The exploration of how the capillary numbers for compound drops affect the drop deformation inside the constriction and their effect on transit time appears to be novel work and extending this to drops with different liquid viscosities would be interesting. Different drop sizes can also be included so that the capillary number of the inner phase plays a bigger role. To learn more about clogging, further experiments at lower capillary numbers, either by using less viscous fluids or a higher surface tension should be done. Experiments with compound drops should also be done. Compound drops that are smaller than what we tried to make can be used, and if making axisymmetric constrictions at smaller scales turns out to be too difficult, results from other constriction geometries would also be worth collecting.

Bibliography

[1] Ali, M. A. et al. “Effect of Microwave Heating on Oxidative Degradation of Sunflower Oil in the Presence of Palm Olein”. In: *Sains Malaysiana* 43 (Aug. 2014), pp. 1189–1195.

[2] Anderson, D. M., McFadden, G. B., and Wheeler, A. A. “Diffuse-interface methods in fluid mechanics”. In: *Annual review of fluid mechanics* 30.1 (1998), pp. 139–165.

[3] Boyer, F. and Lapuerta, C. “Study of a three component Cahn-Hilliard flow model”. In: *ESAIM: Mathematical Modelling and Numerical Analysis* 40.4 (2006), pp. 653–687.

[4] Boyer, F. et al. “Cahn–Hilliard/Navier–Stokes model for the simulation of three-phase flows”. In: *Transport in Porous Media* 82.3 (2010), pp. 463–483.

[5] Bretherton, F. P. “The motion of long bubbles in tubes”. In: *Journal of Fluid Mechanics* 10.2 (1961), pp. 166–188.

[6] C Bauer, W.-A. et al. “Hydrophilic PDMS microchannels for high-throughput formation of oil-in-water microdroplets and water-in-oil-in-water double emulsions”. In: *Lab on a chip* 10 (May 2010), pp. 1814–9.

[7] Cahn, J. W. and Hilliard, J. E. “Free Energy of a Nonuniform System. I. Interfacial Free Energy”. In: *The Journal of Chemical Physics* 28.2 (1958), pp. 258–267.

[8] Calderer, M.-C. T. and Terentjev, E. M. *Modeling of Soft Matter*. The IMA Volumes in Mathematics and its Applications. Springer-Verlag New York, 2005.

[9] Carlson, A., Do-Quang, M., and Amberg, G. “Dissipation in rapid dynamic wetting”. In: *Journal of Fluid Mechanics* 682 (2011), pp. 213–240.

[10] Carlson, A., Do-Quang, M., and Amberg, G. “Droplet dynamics in a bifurcating channel”. In: *International Journal of Multiphase Flow* 36.5 (2010), pp. 397–405.

[11] Carlson, A., Do-Quang, M., and Amberg, G. “Modeling of dynamic wetting far from equilibrium”. In: *Physics of Fluids* 21.12 (2009), p. 121701.

[12] Cobos, S., Carvalho, M., and Alvarado, V. “Flow of oil–water emulsions through a constricted capillary”. In: *International Journal of Multiphase Flow* 35.6 (2009), pp. 507–515.

[13] Cox, R. G. “The deformation of a drop in a general time-dependent fluid flow”. In: *Journal of Fluid Mechanics* 37.3 (1969), pp. 601–623.

[14] Darzi, M. and Park, C. “Optical distortion correction of a liquid-gas interface and contact angle in cylindrical tubes”. In: *Physics of Fluids* 29.5 (2017), p. 052004.

[15] Dawson, G., Häner, E., and Juel, A. “Extreme deformation of capsules and bubbles flowing through a localised constriction”. In: *Procedia IUTAM* 16 (2015), pp. 22–32.

[16] Denais, C. M. et al. “Nuclear envelope rupture and repair during cancer cell migration”. In: *Science* 352.6283 (2016), pp. 353–358.

[17] *Determining the surface tension of liquids by measurements on pendant drops*. https://www.kruss-scientific.com/fileadmin/user_upload/website/literature/kruss-tn316-en.pdf. Accessed: 2019-07-12.

[18] Dondorp, A. M. et al. “Red blood cell deformability as a predictor of anemia in severe falciparum malaria.” In: *The American Journal of Tropical Medicine and Hygiene* 60.5 (1999), pp. 733–737.

[19] Eddi, A., Winkels, K. G., and Snoeijer, J. H. “Short time dynamics of viscous drop spreading”. In: *Physics of Fluids* 25.1 (2013), p. 013102.

[20] Edvinsson, R. K. and Irandoust, S. “Finite-element analysis of Taylor flow”. In: *AIChE Journal* 42.7 (1996), pp. 1815–1823.

[21] Elder, K. R. et al. “Sharp interface limits of phase-field models”. In: *Phys. Rev. E* 64 (2 2001), p. 021604.

[22] Eral, H. B., ’t Mannetje, D. J. C. M., and Oh, J. M. “Contact angle hysteresis: a review of fundamentals and applications”. In: *Colloid and Polymer Science* 291.2 (Feb. 2013), pp. 247–260.

[23] Esteban, B. et al. “Temperature dependence of density and viscosity of vegetable oils”. In: *Biomass and Bioenergy* 42 (2012), pp. 164–171.

[24] Fauli, R. *Github repository containing Python scripts*. https://github.com/richaraf/Squeezing-of-drops-through-constrictions. 2019.

[25] Feng, J. J. et al. “An Energetic Variational Formulation with Phase Field Methods for Interfacial Dynamics of Complex Fluids: Advantages and Challenges”. In: *Modeling of Soft Matter*. Ed. by Calderer, M.-C. T. and Terentjev, E. M. New York, NY: Springer New York, 2005, pp. 1–26.

[26] Glawdel, T., Elbuken, C., and Ren, C. L. “Droplet Generation in Microfluidics”. In: *Encyclopedia of Microfluidics and Nanofluidics*. Ed. by Li, D. Boston, MA: Springer US, 2013, pp. 1–12.

[27] Guido, S. and Villone, M. “Measurement of Interfacial Tension by Drop Retraction Analysis”. In: *Journal of Colloid and Interface Science* 209.1 (1999), pp. 247–250.

[28] Guo, Q. et al. “Microfluidic analysis of red blood cell deformability”. In: *Journal of Biomechanics* 47.8 (2014), pp. 1767–1776.

[29] Hodges, S., Jensen, O., and Rallison, J. “The motion of a viscous drop through a cylindrical tube”. In: *Journal of fluid mechanics* 501 (2004), pp. 279–301.

[30] Hoyt, L. F. “New Table of the Refractive Index of Pure Glycerol at 20°C”. In: *Industrial & Engineering Chemistry* 26.3 (1934), pp. 329–332.

[31] Hu, Y., Zhang, X., and Wang, W. “Boundary Conditions at the Liquid-Liquid Interface in the Presence of Surfactants”. In: *Langmuir : the ACS journal of surfaces and colloids* 26 (July 2010), pp. 10693–702.

[32] Jacqmin, D. “Calculation of Two-Phase Navier–Stokes Flows Using Phase-Field Modeling”. In: *Journal of Computational Physics* 155.1 (1999), pp. 96–127.

[33] Jacqmin, D. “Contact-line dynamics of a diffuse fluid interface”. In: *Journal of Fluid Mechanics* 402 (2000), pp. 57–88.

[34] Jaensson, N., Hulsen, M., and Anderson, P. “Stokes–Cahn–Hilliard formulations and simulations of two-phase flows with suspended rigid particles”. In: *Computers & Fluids* 111 (2015), pp. 1–17.

[35] Jensen, M. J., Goranović, G., and Bruus, H. “The clogging pressure of bubbles in hydrophilic microchannel contractions”. In: *Journal of Micromechanics and Microengineering* 14.7 (2004), p. 876.

[36] Kay, D., Styles, V., and Süli, E. “Discontinuous Galerkin finite element approximation of the Cahn–Hilliard equation with convection”. In: *SIAM Journal on Numerical Analysis* 47.4 (2009), pp. 2660–2685.

[37] Kay, D., Styles, V., and Welford, R. “Finite element approximation of a Cahn-Hilliard-Navier-Stokes system”. In: *Interfaces Free Bound* 10.1 (2008), pp. 15–43.

[38] Kim, J. “A diffuse-interface model for axisymmetric immiscible two-phase flow”. In: *Applied mathematics and computation* 160.2 (2005), pp. 589–606.

[39] Kim, J. “Phase field computations for ternary fluid flows”. In: *Computer methods in applied mechanics and engineering* 196.45-48 (2007), pp. 4779–4788.

[40] Kim, J. et al. “Basic Principles and Practical Applications of the Cahn–Hilliard Equation”. In: *Mathematical Problems in Engineering* 2016 (Jan. 2016), pp. 1–11.

[41] Kusters, R. et al. “Forced transport of deformable containers through narrow constrictions”. In: *Physical Review E* 90.3 (2014), p. 033006.

[42] Lac, E. and Sherwood, J. D. “Motion of a drop along the centreline of a capillary in a pressure-driven flow”. In: *Journal of Fluid Mechanics* 640 (2009), pp. 27–54.

[43] Leal, L. G. *Advanced Transport Phenomena: Fluid Mechanics and Convective Transport Processes*. Cambridge Series in Chemical Engineering. Cambridge University Press, 2007.

[44] Lee, D. et al. “Physical, mathematical, and numerical derivations of the Cahn–Hilliard equation”. In: *Computational Materials Science* 81 (2014), pp. 216–225.

[45] Leong, F. Y. et al. “Modeling cell entry into a micro-channel”. In: *Biomechanics and modeling in mechanobiology* 10.5 (2011), pp. 755–766.

[46] Leyrat-Maurin, A. and Barthes-Biesel, D. “Motion of a deformable capsule through a hyperbolic constriction”. In: *Journal of fluid mechanics* 279 (1994), pp. 135–163.

[47] Li, S. et al. “Rapid Preparation of Highly Reliable PDMS Double Emulsion Microfluidic Devices”. In: *RSC Adv.* 6 (Mar. 2016).

[48] Liang, M. et al. “Minimum applied pressure for a drop through an abruptly constricted capillary”. In: *Microfluidics and Nanofluidics* 19.1 (2015), pp. 1–8.

[49] Liu, J. and Trung Nguyen, N. “Numerical simulation of droplet-based microfluidics-A review”. In: *Micro and Nanosystems* 2.3 (2010), pp. 193–201.

[50] Logg, A., Mardal, K.-A., Wells, G. N., et al. *Automated Solution of Differential Equations by the Finite Element Method*. Ed. by Logg, A., Mardal, K.-A., and Wells, G. N. Springer, 2012.

[51] Lundström, T. S. “Bubble transport through constricted capillary tubes with application to resin transfer molding”. In: *Polymer Composites* 17.6 (1996), pp. 770–779.

[52] Magaletti, F. et al. “The sharp-interface limit of the Cahn–Hilliard/Navier–Stokes model for binary fluids”. In: *Journal of Fluid Mechanics* 714 (2013), pp. 95–126.

[53] Mandal, A. et al. “Characterization of oil- water emulsion and its use in enhanced oil recovery”. In: *Industrial & Engineering Chemistry Research* 49.24 (2010), pp. 12756–12761.

[54] Moxon, C. A., Grau, G. E., and Craig, A. G. “Malaria: modification of the red blood cell and consequences in the human host”. In: *British Journal of Haematology* 154.6 (2011), pp. 670–679.

[55] Nascimento, D. F. do et al. “Flow of Tunable Elastic Microcapsules through Constrictions”. In: *Scientific reports* 7.1 (2017), p. 11898.

[56] Nikolovski, B., Ilić, J., and Sovilj, M. “How to formulate a stable and monodisperse water-in-oil nanoemulsion containing pumpkin seed oil: the use of multiobjective optimization”. In: *Brazilian Journal of Chemical Engineering* 33.4 (2016), pp. 919–931.

[57] Olbricht, W. L. and Kung, D. M. “The deformation and breakup of liquid drops in low Reynolds number flow through a capillary”. In: *Physics of Fluids A: Fluid Dynamics* 4.7 (1992), pp. 1347–1354.

[58] Pawar, Y. and Stebe, K. J. “Marangoni effects on drop deformation in an extensional flow: The role of surfactant physical chemistry. I. Insoluble surfactants”. In: *Physics of Fluids* 8.7 (1996), pp. 1738–1751.

[59] Raab, M. et al. “ESCRT III repairs nuclear envelope ruptures during cell migration to limit DNA damage and cell death”. In: *Science* 352.6283 (2016), pp. 359–362.

[60] Rallison, J. M. “The Deformation of Small Viscous Drops and Bubbles in Shear Flows”. In: *Annual Review of Fluid Mechanics* 16.1 (1984), pp. 45–66.

[61] Riahi, R. et al. “Microfluidics for advanced drug delivery systems”. In: *Current Opinion in Chemical Engineering* 7 (2015). Biological engineering / Materials engineering, pp. 101–112.

[62] Rorai, C. et al. “Motion of an elastic capsule in a constricted microchannel”. In: *The European Physical Journal E* 38.5 (2015), p. 49.

[63] Schwartz, L., Princen, H., and Kiss, A. “On the motion of bubbles in capillary tubes”. In: *Journal of Fluid Mechanics* 172 (1986), pp. 259–275.

[64] Secomb, T. W. “Blood flow in the microcirculation”. In: *Annual Review of Fluid Mechanics* 49 (2017), pp. 443–461.

[65] Shelby, J. P. et al. “A microfluidic model for single-cell capillary obstruction by Plasmodium falciparum-infected erythrocytes”. In: *Proceedings of the National Academy of Sciences* 100.25 (2003), pp. 14618–14622.

[66] Snoeijer, J. H. and Andreotti, B. “Moving Contact Lines: Scales, Regimes, and Dynamical Transitions”. In: *Annual Review of Fluid Mechanics* 45.1 (2013), pp. 269–292.

[67] Taylor, G. I. “The formation of emulsions in definable fields of flow”. In: *Proceedings of the Royal Society of London. Series A, Containing Papers of a Mathematical and Physical Character* 146.858 (1934), pp. 501–523.

[68] Taylor, G. I. “The viscosity of a fluid containing small drops of another fluid”. In: *Proceedings of the Royal Society of London. Series A, Containing Papers of a Mathematical and Physical Character* 138.834 (1932), pp. 41–48.

[69] Teh, S.-Y. et al. “Droplet microfluidics”. In: *Lab Chip* 8 (2 2008), pp. 198–220.

[70] Tezduyar, T. “Finite Element Methods for Fluid Dynamics with Moving Boundaries and Interfaces”. In: vol. 8. Oct. 2004.

[71] Trantidou, T. et al. “Hydrophilic Surface Modification of Pdms for Droplet Microfluidics Using a Simple, Quick and Robust Method Via Pva Deposition”. In: *Microsystems & Nanoengineering* 3 (Apr. 2017), p. 16091.

[72] Utada, A. et al. “Monodisperse Double Emulsions Generated from a Microcapillary Device”. In: *Science (New York, N.Y.)* 308 (May 2005), pp. 537–41.

[73] Vladisavljević, G., Al Nuumani, R., and Nabavi, S. A. “Microfluidic Production of Multiple Emulsions”. In: *Micromachines* 8 (Mar. 2017), p. 75.

[74] World Health Organization. *World malaria report 2018*. (2018).

[75] Wu, T. et al. “The critical pressure for driving a red blood cell through a contracting microfluidic channel”. In: *Theoretical and Applied Mechanics Letters* 5.6 (2015), pp. 227–230.

[76] Yue, P., Zhou, C., and Feng, J. J. “Spontaneous shrinkage of drops and mass conservation in phase-field simulations”. In: *Journal of Computational Physics* 223.1 (2007), pp. 1–9.

[77] Zhang, X., Chen, X., and Tan, H. “On the thin-film-dominated passing pressure of cancer cell squeezing through a microfluidic CTC chip”. In: *Microfluidics and Nanofluidics* 21.9 (2017), p. 146.

[78] Zhang, Z., Chen, X., and Xu, J. “Entry effects of droplet in a micro confinement: Implications for deformation-based circulating tumor cell microfiltration”. In: *Biomicrofluidics* 9.2 (2015), p. 024108.

[79] Zhang, Z., Xu, J., and Drapaca, C. “Particle squeezing in narrow confinements”. In: *Microfluidics and Nanofluidics* 22.10 (2018), p. 120.

[80] Zhang, Z. et al. “Droplet squeezing through a narrow constriction: Minimum impulse and critical velocity”. In: *Physics of Fluids* 29.7 (2017), p. 072102.

[81] Zhang, Z. et al. “Pressure of a viscous droplet squeezing through a short circular constriction: An analytical model”. In: *Physics of Fluids* 30.10 (2018), p. 102004.

[82] Zhang, Z. et al. “The effects of 3D channel geometry on CTC passing pressure–towards deformability-based cancer cell separation”. In: *Lab on a Chip* 14.14 (2014), pp. 2576–2584.

[83] Zhou, C., Yue, P., and Feng, J. J. “Formation of simple and compound drops in microfluidic devices”. In: *Physics of Fluids* 18.9 (2006), p. 092105.

[84] Zhou, C., Yue, P., and J. Feng, J. “Deformation of a compound drop through a contraction in a pressure-driven pipe flow”. In: *International Journal of Multiphase Flow* 34 (Jan. 2008), pp. 102–109.

[85] Zhu, P. and Wang, L. “Passive and active droplet generation with microfluidics: a review”. In: *Lab on a Chip* 17.1 (2017), pp. 34–75.

[86] Zinchenko, A. Z. and Davis, R. H. “Squeezing of a periodic emulsion through a cubic lattice of spheres”. In: *Physics of Fluids* 20.4 (2008), p. 040803.